3D RECONSTRUCTION, CLASSIFICATION AND MECHANICAL CHARACTERIZATION OF MICROSTRUCTURES

by

MUHAMMET ALİ HOCAOĞLU

Submitted to the Graduate School of Engineering and Natural Sciences
in partial fulfillment of
the requirements for the degree of
Master of Science

Sabanci University

Spring 2008

3D RECONSTRUCTION, CLASSIFICATION AND MECHANICAL CHARACTERIZATION OF MICROSTRUCTURES

MUHAMMET ALİ HOCAOĞLU

APPROVED BY

Assoc. Prof. Dr. Mustafa ÜNEL   ....
(Thesis Advisor)

Assist. Prof. Dr. Kemalettin ERBATUR   ....

Assist. Prof. Dr. Ahmet ONAT   ....

Assist. Prof. Dr. Devrim GÖZÜAÇIK   ....

Assist. Prof. Dr. Hakan ERDOĞAN   ....

DATE OF APPROVAL: ....

to my family

aileme

Autobiography

Muhammet Ali Hocaoğlu was born in Istanbul, Turkey in 1983. He received his B.S. degree in Mechatronics from Sabanci University, Istanbul, Turkey in 2006. His research interests include computer vision and vision-based control of robotic manipulators.

The following were published out of this thesis:

- H. Bilen, M. Hocaoglu, E. Ozgur, M. Unel, and A. Sabanovic, A Comparative Study of Conventional Visual Servoing Schemes in Microsystem Applications, *Proceedings of IEEE/RSJ International Conference on Intelligent Robots and Systems (IEEE IROS 2007)*, 2007, 1308-1313.

- M. Hocaoglu, H. Bilen, E. Ozgur, and M. Unel, Model-Based vs. Model-Free Visual Servoing: A Performance Evaluation in Microsystems, *Proceedings of the 13th IASTED International Conference on Robotics and Applications*, Wuerzburg, Germany, August 29-31, 2007.

- M. Hocaoglu, M. Unel, HK Segmentation of 3D Micro-structures Reconstructed from Focus, D.-S Huang et al. (Eds.) ICIC 2008, LNCS, 5226, 1200-1207, Springer, Heidelberg, 2008.

- H. Bilen, M. Hocaoglu, E. Ozgur, and M. Unel, Gorsel Geri Beslemeli Kontrol Tekniklerinin Mikrosistem Uygulamalarinda Karsilastirilmasi, *TOK'07 Otomatik Kontrol Ulusal Toplantisi Bildiriler Kitabi*, 2007, 529-534.

Acknowledgments

First, I would like to thank my thesis advisor Assoc. Prof. Dr. Mustafa Ünel for his great support, motivation and guidance during my thesis research.

Among all members of the Faculty of Engineering and Natural Sciences, I would gratefully acknowledge Assist. Prof. Dr. Kemalettin Erbatur, Assist. Prof. Dr. Ahmet Onat, Assist. Prof. Dr. Devrim Gözüaçık and Assist. Prof. Dr. Hakan Erdoğan for spending their valuable time to serve as my jurors. Also, I would like to thank Prof. Dr. Asif Sabanovic for his support.

I would also like to acknowledge the support provided by Sabanci University Internal Grant No. IACF06-00417 and TÜBİTAK BİDEB.

Among my friends, first, I would like to thank Meltem Elitaş, Hakan Bilen, Merve Acer and Erol Özgür, who were always next to me and supported me. Also, I would like to thank Kazım Çakır, Emrah Deniz Kunt and Ahmet Teoman Naskali for sharing their knowledge with me.

Finally, I would like to express my gratitude to my family since they always stimulated me during my study.

3D RECONSTRUCTION, CLASSIFICATION AND MECHANICAL CHARACTERIZATION OF MICROSTRUCTURES

Muhammet Ali HOCAOĞLU

Mechatronics Engineering, MS Thesis, 2008

Thesis Supervisor: Assoc. Prof. Dr. Mustafa ÜNEL

Abstract

Modeling and classifying 3D microstructures are important steps in precise micromanipulation. This thesis explores some of the visual reconstruction and classification algorithms for 3D microstructures used in micromanipulation. Mechanical characterization of microstructures has also been considered. In particular, visual reconstruction algorithm (shape from focus - SFF) uses 2D image sequence of a microscopic object captured at different focusing levels to create a 3D range image. Then, the visual classification algorithm takes the range image as an input and applies a curvature-based segmentation method, HK segmentation, which is based on differential geometry. The object is segmented into surface patches according to the curvature of its surface. It is shown that the visual reconstruction algorithm works successfully for synthetic and real image data. The range images are used to classify the surfaces of the micro objects according to their curvatures in the HK segmentation algorithm. Also, a mechanical property characterization technique for cell and embryo is presented. A zebrafish embryo chorion is mechanically characterized using cell boundary deformation. Elastic modulus and developmental stage of the embryo are obtained successfully using visual information. In addition to these, calibrated image based visual servoing algorithm is experimentally evaluated for various tasks in micro domain. Experimental results on optical system calibration and image-based visual servoing in micropositioning and trajectory following tasks are presented.

MİKROSKOPİK YAPILARIN 3B REKONSTRÜKSİYONU, SINIFLANDIRILMASI VE MEKANİK NİTELENDİRİLMESİ

Muhammet Ali HOCAOĞLU

Mekatronik Mühendisliği, Yüksek Lisans Tezi, 2008

Tez Danışmanı: Doç. Dr. Mustafa ÜNEL

Anahtar Kelimeler: Görsel geri beslemeli kontrol, rekonstrüksiyon, sınıflandırma, nitelendirme, mikrosistemler

Özet

3B mikroskopik yapıların modellenmesi ve sınıflandırılması hassas mikromanipülasyonda önemli aşamalardır. Bu çalışmada, bazı görsel rekonstrüksiyon ve sınıflandırma algoritmaları, mikromanipülasyonda kullanılan 3B mikroskopik yapılar üzerinde değerlendirilmiştir. Ayrıca mikroskopik yapıların mekanik nitelendirilmesi de ele alınmıştır. Özellikle, görsel rekonstrüksiyon algoritması (Odak bilgisi üzerinden şekil - SFF) 3B uzaklık imgesi elde etmek için bir mikroskopik nesnenin farklı odaklama seviyelerinde yakalanarak elde edilen 2B imge dizisini kullanır. Sonra, görsel sınıflandırma algoritması giriş olarak uzaklık imgesini alır ve türevsel geometriye dayalı olan eğrilik tabanlı bölütleme metodunu, HK bölütlemesi, kullanır. Nesne, yüzeyinin eğriliğine göre yüzey yamalarına bölütlenir. Görsel rekonstrüksiyon algoritmasının yapay ve gerçek imge verisi üzerinde başarılı bir şekilde çalıştığı gösterilmiştir. Uzaklık imgeleri mikroskopik nesnelerin yüzeylerinin eğriliklerine göre HK bölütleme algoritması ile sınıflandırılmalarında kullanılmıştır. Ayrıca hücre ve embriyo için bir mekanik özellik nitelendirme tekniği sunulmuştur. Bir zebra balığının embriyo koryonu hücre sınırı deformasyonu kullanılarak mekanik olarak nitelendirilmiştir. Embriyonun elastik modülü ve gelişimsel evresi, görsel bilgi kullanarak başarılı bir şekilde elde edilmiştir. Bunlara ek olarak, kalibre edilmiş imge tabanlı görsel geri beslemeli kontrol algoritmalarının performansı, mikro ölçekteki çeşitli uygulamalarda deneysel olarak değerlendirilmiştir. Optik sistem kalibrasyonu ve imge tabanlı görsel geri beslemeli kontrolün mikro konumlandırma ve yörünge takibi uygulamalarında kullanılması ile ilgili deneysel sonuçlar sunulmuştur.

Table of Contents

List of Figures

List of Tables

Chapter 1

Introduction

There is a trend of miniaturization in mass-produced products like sensors, actuators, disk drives and displays [1]. Some of these products are fabricated using very large scale integrated circuit (VLSI) production techniques. However, due to the fact that these devices are mostly composed of integrated circuits (IC) and micro electro mechanical systems (MEMS), which includes microscopic parts, it is not possible to employ industrial robots which have a precision of $100\mu m$ at most. For now, there is not any solution for mass production of products including microscopic electrical and mechanical components and the production is mostly done manually under a microscope. In addition to these, mechanics of object interactions at micro scale is very different. Gravitational forces become ineffective and adhesive forces start to dominate.

The use of visual feedback in micromanipulation of such components can be a solution for the production of micro scale devices. In the control of micromanipulators, like microrobots or micro translational stages, instead of using conventional sensors like motor encoders, computer vision information can be employed. Vision-based control of micromanipulation enables us to disregard adhesive forces generated due to scaling since the manipulation environment is observed by an optical microscope plus camera system and the errors generated by such forces can be easily detected.

In addition to use of visual data in control, it can also be employed in visual reconstruction of manipulation environment and microscopic objects. Due to the low depth of field problem in microscopes, it is not possible to observe all sections of an object. Some parts of the object are not in focus and the images of such parts are not sharp, which creates a loss of visual information. So, employing 3D

reconstruction techniques on microscopic object images will ensure more precise micromanipulation.

It is important to extract meaningful models from visual data and classify the objects in the micromanipulation environment. In order to achieve this goal, an image segmentation technique has to be employed. Since 3D image data would be segmented using a classification algorithm specific to range images, typical 2D image segmentation techniques do not work for that case. A curvature-based segmentation technique based on differential geometry can be used to discriminate the objects from each other. This segmentation is very important for object recognition at micro scale.

Another application area of computer vision is biomicromanipulation. A proper microinjection and cell diagnosis necessitates mechanical characterization of cells/ embryos. However, for the cells it is not possible to apply characterization techniques used for macro scale objects. Visual data combined with force sensor measurement can be employed to mechanically characterize the cells. The characterization result can also be used to diagnose the cells and learn whether they are infected or not.

1.1 Contribution of the Thesis

In this thesis visual information is employed in micromanipulator control, visual reconstruction and classification of microscopic objects, and characterization of cells. Calibrated image based visual servoing algorithm is evaluated in micropositioning and trajectory following tasks. Microscopic objects are reconstructed using focus information and their range images are obtained. Resulting range images are used in a curvature-based segmentation (HK segmentation) algorithm to recognize the objects. In addition to these, mechanical property characterization of biological cells/tissues such as an embryo is outlined.

1.2 Organization of the Thesis

The remaining parts of the thesis are organized as follows: Chapter 2 summarizes characteristics of microsystems, visual servoing techniques and optical system calibration. Chapter 3 presents visual reconstruction and classification methods. Chap-

ter 4 introduces mechanical property characterization of an embryo using biomembrane point load model. Chapter 5 presents experimental results performed on a microassembly workstation and discussions. Chapter 6 concludes the thesis with some remarks and proposes some future works.

Chapter 2

Microsystems and Vision

Micromanipulation differs from object manipulation in macro world due to the high precision requirements and mechanics of micromanipulation. The problems caused by characteristics of micro world can be resolved by utilizing real-time visual feedback. In this chapter, characteristics of micromanipulation is examined and image based calibrated visual servoing approach is employed to compensate uncertainties in microsystems.

2.1   Characteristics of Microsystems

Micromanipulation lies between macro-scale manipulation and nano-manipulation [1], as illustrated in Fig. 2.1. Currently, there is not a generalized solution for automatic micromanipulation/assembly due to the specific problems related to micro world. One of the major differences between macro and micro manipulation is the
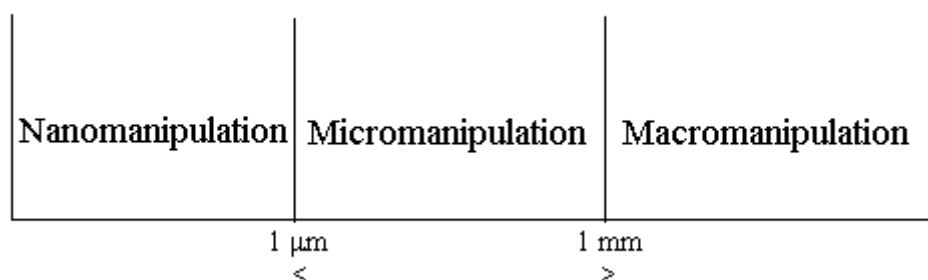

Figure 2.1: Scale of Micromanipulation

required positional accuracy for the manipulators. Although a precision of a few hundred microns is typical for a robotic manipulator in the macro domain, for the

applications in the micro domain, submicron precision is required and this degree of precision is beyond the capability of the assembly devices used in the industry due to the fact that precise calibration of these devices is necessary to achieve high accuracy. According to Nelson et al. [2] precise calibration of these devices is highly dependent on precisely modeled kinematics which are subject to thermal growth errors and these errors are typically the most difficult to control and compensate in precision machine design as Slocum [3] mentioned.

In addition to the different precision requirements, the mechanics of object interactions is different for macro and micro assembly. In macro world, the mechanics of manipulation are predictable to a degree since the forces due to gravity are dominant. However, in the micro world, due to the scaling effects, forces that are not significant in the macro world become dominant [4], [5]. For example, when the parts to be handled are less than one millimeter in size, adhesive forces between gripper and object can be significant compared to gravitational forces. These adhesive forces, caused primarily from surface tension, van der Waals forces and electrostatic attractions, can be a fundamental limitation to part handling as shown in Fig. 2.2. Surface tension arises from interaction of layers of absorbed moisture on two surfaces. Van der Waals forces are caused by instantaneous polarization of atoms and molecules due to quantum mechanical effects. Electrostatic attractions are due to charge generation or charge transfer during contact [1].

As described in [6], in micromanipulation, electrostatic forces can dominate and cause a part to jump into a microgripper before contact actually occurs. When the microgripper opens to place the micropart at its goal, the part may stick to the microgripper fingers due to van der Waals and/or electrostatic forces. If humidity in the room happens to be high, surface tension effects can dominate gravitational forces, and the part would remain stuck to the gripper. Since, it is hard to model and estimate micro-scale forces and precise calibration of robotic manipulators is highly dependent on precisely modeled kinematics which are subject to thermal growth errors, real-time visual feedback can be used effectively and economically as a component of a micromanipulation system.

Employing visual feedback effectively in the control loop of a micromanipulation process presents challenges quite different from those presented in macro scale. First
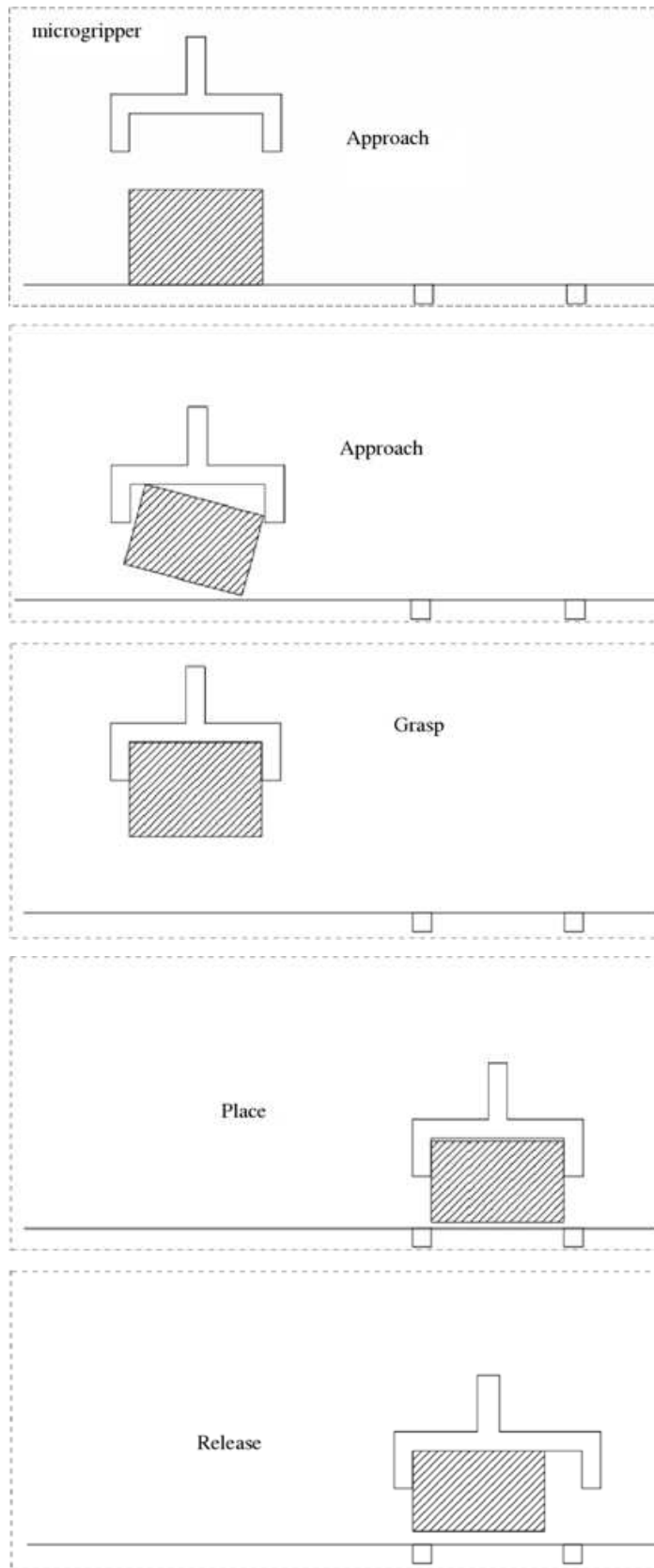
Figure 2.2: Sticking Effects in Micromanipulation

difficulty in the micro world is the optical system calibration which is a vital step for visual servoing applications because the parameters of the optical system are used in image based visual servoing for image Jacobian computation. Since optical microscope calibration has its unique characteristics, it introduces challenges that are different from conventional camera calibration. Another important problem is visual tracking since the objects generally do not have simple local features such as line segments, edges or contours in the micro world and a micromanipulator moving in an unknown environment can be tracked by a template-based tracking algorithm. These solutions were employed in the application of image based visual servoing in micromanipulation as done in [10], [11].

2.2 Visual Servoing

Using visual feedback to control a robotic manipulator is termed as visual servoing [7]. Image features like points, lines or regions are used to enable the alignment of a manipulator with an object. Use of visual servoing increases flexibility in the manipulation.

Closed-loop control of a robotic manipulator is composed of feature extraction from tracking and use of these features to control the manipulator. The manipulator can be controlled using either two dimensional or three dimensional image features. Image-based visual servoing (IBVS) employs 2D image measurements to estimate the desired movement of the robot. Tasks like tracking and positioning are achieved by reducing the image distance error between current image features and desired image features. On the other hand, position-based visual servoing (PBVS) employs 3D information about a scene where camera calibration information is used to obtain position and orientation of an object with respect to camera coordinate system. Positioning and tracking is defined in terms of 3D coordinates [8]. Real-time 3D reconstruction of the scene is very challenging in micromanipulation due to the fact that microscopes have low depth-of-field, which causes only some parts of the scene to be in focus. In addition to that in most cases there is not a 3D model of the microscopic object to be used in pose estimation. So, IBVS employing dynamic look and move structure, shown schematically in Fig. 2.3, is preferred to control the manipulators. In this structure, input to control law is obtained using vision

information, then the output of control law is used by robot controller which employs joint feedback to internally stabilize the robot.
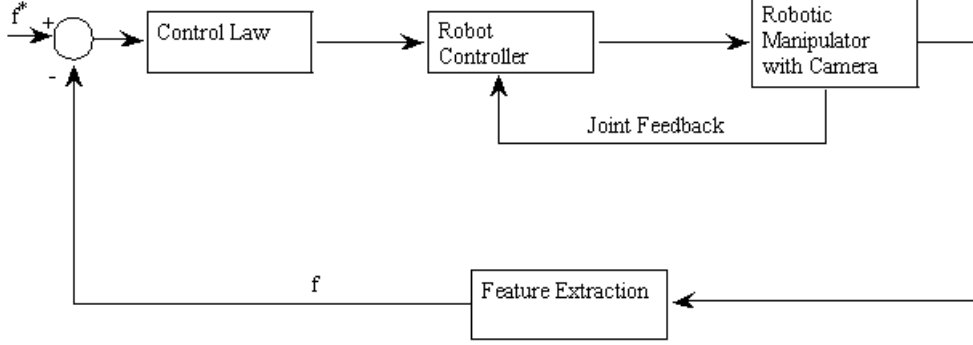
Figure 2.3: Image-Based Visual Servoing Scheme

In image based visual servoing, for a case of moving target and a constant desired feature value f^* [9], error is defined in the following way,

$$e = f - f^* \qquad (2.1)$$

where f is a vector of image features related to the moving target. The time variation of the error can be given as:

$$\dot{e} = \dot{f} = J\dot{r} + \frac{\partial e}{\partial t} \qquad (2.2)$$

where J is the image Jacobian matrix which is a function of the visual features and intrinsic/extrinsic parameters of the visual sensor, $\dot{r}$ is a velocity screw in the task space, and $\frac{\partial e}{\partial t}$ is the time variation of e due to the unknown target motion. In order to ensure exponential decrease of e ($\dot{e} = -\lambda e$), control law can be designed using (2.2) as follows:

$$\dot{r} = -\lambda \widehat{J^+} e - \widehat{J^+} \widehat{\frac{\partial e}{\partial t}} \qquad (2.3)$$

where $\widehat{\frac{\partial e}{\partial t}}$ is an approximation of $\frac{\partial e}{\partial t}$ and $\widehat{J^+}$ is an estimate of pseudo-inverse of Jacobian matrix. The term $\widehat{\frac{\partial e}{\partial t}}$ is introduced to compensate for target motion. In light of (2.3), (2.2) can be modified as follows:

$$\dot{e} = -\lambda J\widehat{J^+} e - J\widehat{J^+}\widehat{\frac{\partial e}{\partial t}} + \frac{\partial e}{\partial t} \qquad (2.4)$$

If $J\widehat{J^+} > 0$ and estimation $\widehat{\frac{\partial e}{\partial t}}$ is sufficiently accurate, error will converge to zero.

8

In IBVS, Jacobian matrix can be computed analytically via calibrating the optical system.

2.2.1 Calibration of the Optical System

In the calibration procedure, the intrinsic optical system parameters, which are tube length of the microscope (T_{op}), objective focal length (f), radial distortion (κ), distance of the object plane to the front focal plane (d), and the extrinsic optical system parameters, which are rotation (R) and translation (T) of world coordinate frame to objective coordinate frame must be computed.

Several calibration methods exist in the literature that are mostly used in macro scale vision applications [12]- [14]. However, these methods cannot be utilized without modifications in the calibration of an optical microscope due to its unique characteristics. High-resolution microscope optics means large numerical apertures and high optical magnifications, thus a very small depth-of-field. The position of micromanipulator and the geometry of micro object can lead to several focal planes in the limited depth of field. Therefore, only a calibration pattern which is parallel to the image plane of the objective could be used. Due to the fact that calibration algorithm proposed in [12] requires the calibration pattern to be tilted at least 30° according to the image plane and the calibration techique in [13] needs at least three images of the calibration pattern at different orientations that requires rotation in x and y axis, these methods can not be proposed as a direct solution to the calibration of the optical system. The camera calibration for a near parallel case is proposed in [15] under the assumption of small rotations of the camera about x and y axes, rotation angles around these axes, which are γ and β respectively, were linearized to simplify the extraction of the extrinsic parameters by the small angle approximation. However, this model cannot give accurate rotation angles and needs pre-calibration of the focal length which is not possible for the optical system. The calibration of an optical microscope has been carried out by Zhou and Nelson based on a Tsai's model and specially modified for the parallel case [16].

Zhou and Nelson's calibration method was validated on (optical microscope + camera) system. The importance of the calibration is that the intrinsic parameters are used in the image Jacobian matrix and thus it is vital for image based visual

servoing.

A. Parametric Model for an Optical Microscope

Perspective projection of a world point on calibration pattern plane onto the virtual image plane is presented in Fig. 2.4. There are three coordinate system assignments which are objective coordinate system C_o, image coordinate system C_i, and world coordinate system C_w. Since calibration pattern plane is parallel to the image plane, it is assumed that $Z_w = 0$ for all points on the pattern. Extrinsic parameters of
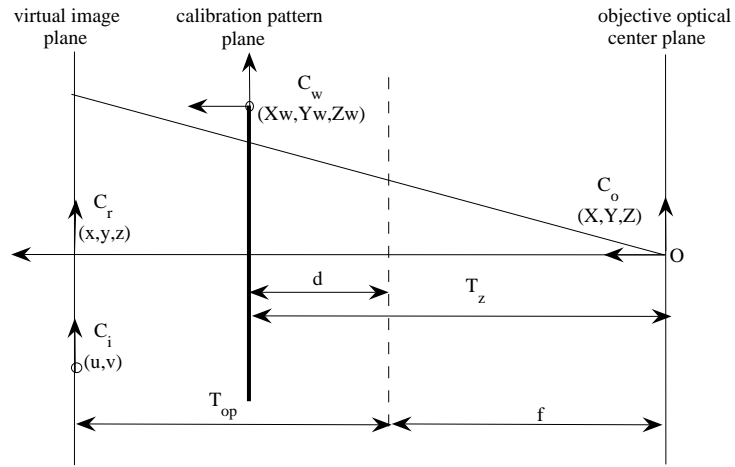
Figure 2.4: Parametric Microscope Model

calibration are transformation T and rotation R from world coordinate system to objective coordinate system which are given as

$$
\begin{bmatrix} X \\ Y \\ Z \end{bmatrix} = \begin{bmatrix} r_{11} & r_{12} & r_{13} \\ r_{21} & r_{22} & r_{23} \\ r_{31} & r_{32} & r_{33} \end{bmatrix} \begin{bmatrix} X_w \\ Y_w \\ Z_w \end{bmatrix} + \begin{bmatrix} T_x \\ T_y \\ T_z \end{bmatrix} \tag{2.5}
$$

where R is a function of the three Euler angles α, β, γ:

$$
R = \begin{bmatrix} cos\alpha cos\beta & cos\alpha sin\beta sin\gamma - sin\alpha cos\gamma & cos\alpha sin\beta cos\gamma + sin\alpha sin\gamma \\ sin\alpha cos\beta & sin\alpha sin\beta sin\gamma + cos\alpha cos\gamma & sin\alpha sin\beta cos\gamma - cos\alpha sin\gamma \\ -sin\beta & cos\beta sin\gamma & cos\beta cos\gamma \end{bmatrix} \tag{2.6}
$$

10

Rotation matrix is obtained by three successive rotations, which are γ degrees around x axis, β degrees around y axis, and α degrees around z axis,

$$R = R_{z,\alpha} R_{y,\beta} R_{x,\gamma} \tag{2.7}$$

Since the calibration pattern plane is nearly parallel with the image plane, it is assumed that $T_z \approx f + d$ and T is reformulated as:

$$T = \begin{bmatrix} T_x \\ T_y \\ f+d \end{bmatrix} \tag{2.8}$$

As a result of the perspective projection, the undistorted image coordinates (u',v') of the pattern are obtained as:

$$u' = (T_{op} + f)\frac{X}{Z}$$

$$v' = (T_{op} + f)\frac{Y}{Z} \tag{2.9}$$

Due to the fact that the microscope lenses are manufactured precisely, only first radial distortion coefficient κ is considered:

$$u' = u(1 + \kappa r^2)$$

$$v' = v(1 + \kappa r^2) \tag{2.10}$$

where $r = \sqrt{u^2 + v^2}$, and (u, v) are distorted image coordinates.

Using (2.5)-(2.10), the relation between world coordinates and image coordinates is obtained as

$$u(1 + \kappa r^2) = (T_{op} + f)\frac{r_{11}X_w + r_{12}Y_w + T_x}{r_{31}X_w + r_{32}Y_w + f + d}$$

$$v(1 + \kappa r^2) = (T_{op} + f)\frac{r_{21}X_w + r_{22}Y_w + T_y}{r_{31}X_w + r_{32}Y_w + f + d} \tag{2.11}$$

The magnification of the optical system is given as

$$M = \frac{T_{op}}{f} = \frac{T_{op} + f}{f + d} \tag{2.12}$$

Intrinsic and extrinsic parameters of the optical system are calculated using (2.11)-(2.12).

B. Algorithm for Optical System Calibration

Calibration algorithm in [16] is used to calibrate the optical system. The algoritm is composed of two steps. In the first step extrinsic parameters are obtained through a closed-form solution. Then, in the second step intrinsic parameters are calculated using nonlinear minimization.

Radial Alignment Constraint(RAC) introduced by Tsai [12] is employed in the first step to evaluate the rotation angles (α, β, γ) and T_x and T_y components of the translation vector, T. According to RAC, the vector extending from the origin in the image plane to the image point radially aligned with the vector extending from the optical axis to the object point. This constraint can be formulated as

$$(u, v) \times (X, Y) = uY - vX = 0 \tag{2.13}$$

In light of (2.5), (2.13) becomes,

$$u(r_{21}X_w + r_{22}Y_w + T_y) = v(r_{11}X_w + r_{12}Y_w + T_x) \tag{2.14}$$

(2.14) can be transformed into a linear form as

$$u = \begin{bmatrix} uX_w & vY_w & v & -uX_w & vY_w \end{bmatrix} \begin{bmatrix} Ty^{-1}r_{11} \\ Ty^{-1}r_{12} \\ Ty^{-1}T_x \\ Ty^{-1}r_{21} \\ Ty^{-1}r_{22} \end{bmatrix} \tag{2.15}$$

A solution for (2.15) can be found using singular value decomposition (SVD). After applying some algebraic manipulations on the solution as done in [12], the extrinsic parameters, excluding T_z, can be estimated.

In the second step of the calibration, first, an initial value is estimated for f and T_z. (2.11) is reformulated using the assumption that calibration pattern is parallel to the image plane as

$$u(1 + \kappa r^2) = (T_{op} + f)\frac{r_{11}X_w + r_{12}Y_w + T_x}{f + d}$$

$$v(1 + \kappa r^2) = (T_{op} + f)\frac{r_{21}X_w + r_{22}Y_w + T_y}{f + d} \tag{2.16}$$

Let

$$p = r_{11}X_w + r_{12}Y_w + T_x$$

$$q = r_{21}X_w + r_{22}Y_w + T_y \tag{2.17}$$

Combining (2.12), (2.16) and (2.17), a relation between image points and intrinsic parameters can be obtained as

$$\frac{T_{op}}{f}(p+q) - \kappa(u+v)r^2 = u+v \tag{2.18}$$

(2.18) can be formulated as a linear system as

$$u + v = \begin{bmatrix} p+q & \kappa(u+v)r^2 \end{bmatrix} \begin{bmatrix} \frac{T_{op}}{f} \\ \kappa \end{bmatrix} \tag{2.19}$$

Using sufficient number of calibration points, a solution for unknowns $\frac{T_{op}}{f}$ and κ can be estimated using SVD. Since microscope objectives are precisely manufactured, f value given by manufacturer can be used as an initial estimate. Using that estimate T_{op} can be evaluated. Reformulating (2.12) as

$$d = \frac{f^2}{T_{op}} \tag{2.20}$$

d can be calculated. Using the initial estimates for f, T_{op}, κ, and d in a nonlinear optimization, final values of intrinsic parameters can be obtained.

2.2.2 Derivation of the Image Jacobian

Let (X, Y, Z) denote the objective frame coordinates of an observed feature point P. Locating the image coordinate frame at the center of the CCD array and assuming weak perspective projection, the undistorted image coordinates (x'_s, y'_s) in objective frame are given as

$$x'_s = MX, \ y'_s = MY, \tag{2.21}$$

where $M = \frac{T_{op}+f}{f+d}$ is the total magnification of the optical system.

Since the lens radial distortion parameter (κ) is very small, the distorted image coordinates (x_s, y_s) in pixels can be written as

$$x_s \approx x'_s = \frac{M}{s_x}X, \ \ y_s \approx y'_s = \frac{M}{s_y}Y \tag{2.22}$$

where s_x and s_y are the effective pixel sizes.

The optical flow equations can be obtained by differentiating (2.22) with respect to time

$$\dot{x}_s = \frac{M}{s_x}\dot{X}, \ \ \dot{y}_s = \frac{M}{s_y}\dot{Y} \tag{2.23}$$

13

Assume that the point P is rigidly attached to the end effector of the manipulator and moves with an angular velocity $\Omega = (\omega_x, \omega_y, \omega_z)$ and a translational velocity $V = (V_x, V_y, V_z)$. The motion in the objective frame is given by

$$
\begin{pmatrix} \dot{X} \\ \dot{Y} \\ \dot{Z} \end{pmatrix} = \begin{pmatrix} V_x \\ V_y \\ V_z \end{pmatrix} + \begin{pmatrix} 0 & -\omega_z & \omega_y \\ \omega_z & 0 & -\omega_x \\ -\omega_y & \omega_x & 0 \end{pmatrix} \begin{pmatrix} X \\ Y \\ Z \end{pmatrix} \tag{2.24}
$$

Substituting (2.24) into (2.23) and using (2.22) implies

$$
\begin{pmatrix} \dot{x}_s \\ \dot{y}_s \end{pmatrix} = \underbrace{\begin{pmatrix} \frac{M}{s_x} & 0 & 0 & 0 & \frac{M}{s_x}Z & -\frac{s_y}{s_x}y_s \\ 0 & \frac{M}{s_y} & 0 & -\frac{M}{s_y}Z & 0 & \frac{s_x}{s_y}x_s \end{pmatrix}}_{\triangleq J} \begin{pmatrix} V_x \\ V_y \\ V_z \\ \omega_x \\ \omega_y \\ \omega_z \end{pmatrix} \tag{2.25}
$$

where J is the Jacobian for a point feature.

2.2.3 Visual Controller Synthesis

Assuming $\frac{\partial e}{\partial t} = 0$ since the object position information is estimated from feature tracking, (2.2) can be written in discrete time as

$$
f(k+1) = f(k) + TJ(k)u(k) \tag{2.26}
$$

where $f \in \mathbb{R}^{2N}$ is the vector of image features being tracked, N is the number of the features, T is the sampling time of the vision sensor, and $u(k)$ is the velocity vector of the end effector.

The aim of the visual servoing tasks in the experiments is to locate the end effector to a constant or time varying desired target $f^*(k)$ by controlling its velocity. A cost function as in [11] is introduced to penalize the pixelized position errors and the control energy as

$$
E(k+1) = (f(k+1) - f^*(k+1))^T Q(f(k+1) - f^*(k+1))
$$

$$
+ u^T(k)Lu(k) \tag{2.27}
$$

14

The resulting optimal control input $u(k)$ can be derived as

$$u(k) = -(TJ^T(k)QTJ(k) + L)^{-1}TJ^T(k)Q(f(k) - f^*(k+1)) \qquad (2.28)$$

The weighting matrices Q and L can be adjusted to ensure desired response.

Chapter 3

Visual Reconstruction and Classification

Precise micromanipulation requires 3D shape and surface structure of the manipulated object. Conventional 3D reconstruction techniques like structured light, binocular stereo and shape from shading do not give proper results for microscopic objects. In order to have a precise reconstruction in the micro domain, shape from focus (SFF) algorithm is proposed in [20] and further improvements are done on the algorithm using different focus measures and evaluation methods in [21] - [25]. The acquisition of the 3D geometry of micro object enables us to apply a curvature-based descriptor to obtain range surface segmentation. Curvature-based desriptors were used in several applications like object classification, pose estimation, and computer graphics. Besl applied HK segmentation on range images of several objects and scenes, and fitted variable-order surfaces to the segmentation results [28]. Trucco and Fisher evaluated range image segmentation system using estimates of the sign of the mean and Gaussian curvatures (H and K respectively) on a range image of an automobile part [30]. Moreno et.al applied HK segmentation on 3D human face surfaces for face recognition [31].

In the literature, the problem of extracting surface information from range images of macro scale objects is addressed. In this chapter, the problem of visual reconstruction and classification of microscopic objects is examined. Shape of the object is recovered using SFF technique. Then using the resulting shape from this process, curvature-based segmentation of the range image is realized.

3.1   Visual Reconstruction

Visual reconstruction is achieved using focus information of the images. In the reconstruction procedure, focused and defocused images of an object are captured at different focusing levels. Using a proper focus measure in SFF algorithm, 3D map of the object is acquired.

3.1.1   Image Formation in Microscopy

Microscope objective is assumed as a thin lens as shown in Fig. 3.1. Light rays radiating from object point O and intercepting by the lens are refracted by the lens to converge at the point C on the image plane. According to the Gaussian lens law, the relation between object distance d_o, image distance d_i and focal length f is given as:

$$\frac{1}{d_o} + \frac{1}{d_i} = \frac{1}{f} \tag{3.1}$$

Each point on the object plane is projected on a point on the image plane. This results in a focused image $I(x, y)$. However, if sensor plane and image plane do not coincide, the image of a point on the sensor plane will be a circular blob of radius r_b.

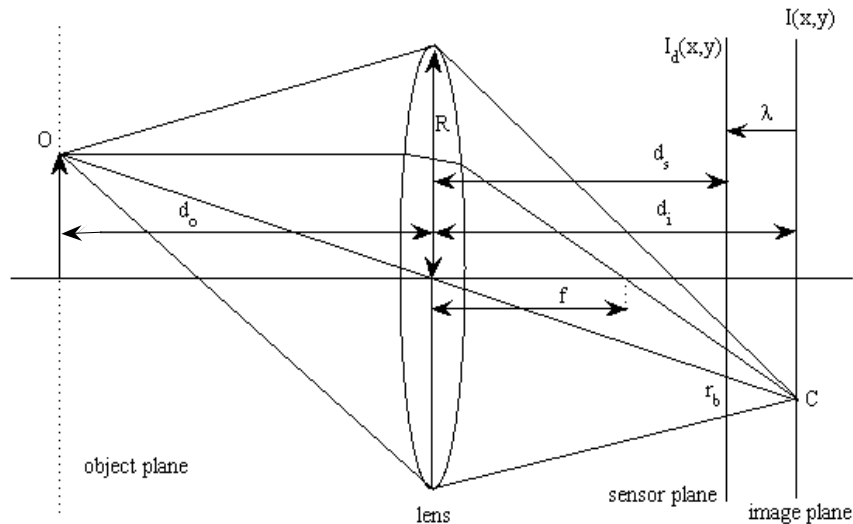According to Fig. 3.1, the relation between r_b and the sensor displacement, λ,

Figure 3.1: Formation of focused and defocused images in microscope

can be given as

$$r_b = R\lambda/d_i \tag{3.2}$$

where

$$\lambda = d_i - d_s \tag{3.3}$$

Using the Gaussian lens law, the blur radius can be reformulated as [27]:

$$r_b = Rd_s[1/d_s + 1/d_o - 1/f] \tag{3.4}$$

Supposing $1/w_d = 1/f - 1/d_s$, (3.4) becomes

$$r_b = Rd_s[1/d_o - 1/w_d] \tag{3.5}$$

where w_d is working distance of the microscope objective. If an object point is at a distance d_o which is equal to w_d then it forms a focused image.

The blur in the circular blob can be modeled using a 2-D Gaussian function [26]. Thus, defocused image $I_d(x, y)$ on the sensor plane can be described as the result of convolution of the Gaussian function $g(x, y)$ and the focused image $I(x, y)$:

$$I_d(x, y) = g(x, y) * I(x, y) \tag{3.6}$$

where

$$g(x, y) = \frac{1}{2\pi\sigma_g^2} e^{-\frac{x^2+y^2}{2\sigma_g}} \tag{3.7}$$

Standard deviation of the function, σ_g, is proportional to the blur radius r_b [26].

Defocusing process can be expressed in the frequency domain if we take the Fourier transform of (3.6):

$$I_D(u, v) = G(u, v)I(u, v) \tag{3.8}$$

where

$$G(u, v) = e^{-\frac{u^2+v^2}{2}\sigma_g^2} \tag{3.9}$$

$G(u, v)$ low-pass filters the focused image $I(u, v)$. As the sensor displacement λ increases, blur radius r_b increases, and the standard deviation of the function σ_g increases. So, high frequency content in $I(u, v)$ is attenuated. Loss of high frequency elements in the image results in a loss of texture information and sharpness.

3.1.2   Shape from Focus

A microscopic object with an unknown shape is placed on a micro-translational stage under the optical microscope as shown in Fig. 3.2. Initially, background of the object is at the focused plane, and the distance between the microscope objective and points on the background is working distance. Then, the stage is moved in increments of Δd and at each increment the surface element S gradually comes into focus. A sequence of images are captured at each increment to estimate depth of the surface element. When the displacement $d = d_s$, where d_s is height of the surface element S, the surface element comes into maximum focus. In Fig. 3.2, $d > d_s$, so, the surface element S is not in focus. This procedure is applied for all surface elements on the object.
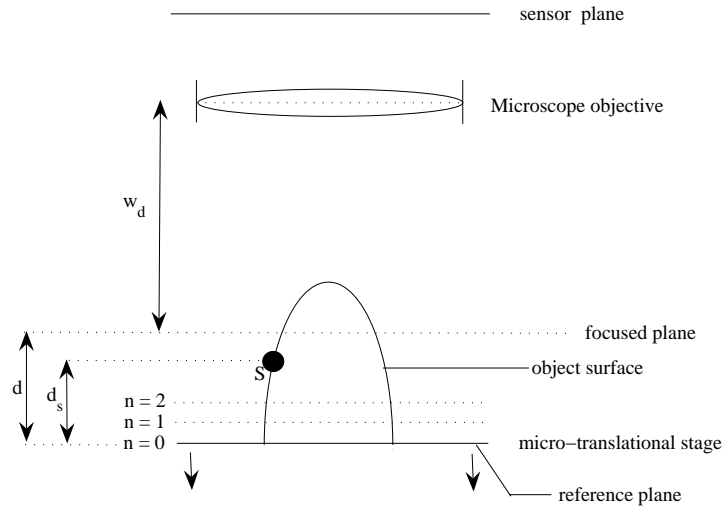
Figure 3.2: Shape Estimation from Focus

A. Focus Measure Selection

In order to evaluate the degree of focus, a focus measure, which would high-pass filter the defocused image [20], has to be selected. The focus measure is calculated in a region around each pixel in the image sequence and the operator gives the highest value at the image which object point is in maximum focus. In order to high-pass filter the image, Laplacian, which would take second derivative of the image can be used. However, in textured images, the second derivative in x and y directions

would cancel each other. So, to avoid such a problem, modified Laplacian operator given as

$$\nabla_M^2 I = \left| \frac{\partial^2 I}{\partial x^2} \right| + \left| \frac{\partial^2 I}{\partial y^2} \right| \tag{3.10}$$

is used. Discrete version of (3.10) is a 3×3 operator which is as follows:

$$ML(u,v) = |2I(u,v) - I(u - step, v) - I(u + step, v)|$$

$$+ |2I(u,v) - I(u, v - step) - I(u, v + step)| \tag{3.11}$$

where step is the variable spacing between the pixels. The focus measure at a point (i, j) is computed as the sum of modified Laplacian (SML) values, in a small window around (i, j), using only values that are greater than a threshold:

$$F(i,j) = \sum_{u=i-W}^{i+W} \sum_{v=j-W}^{j+W} ML(u,v), \ \ if \ ML(u,v) > T \tag{3.12}$$

where W determines the window size around the pixel (i,j) to compute the focus measure and T is the threshold value. A small window size of 3×3 or 5×5 is used since large window size introduces blur by taking into account more pixel values which might be quite different from the pixel in consideration as mentioned in [23]. Computation of $F(i,j)$ at each pixel in the image sequence forms a focus measure profile from which depth can be estimated using Gaussian interpolation.

B. Gaussian Interpolation for Focus Measure

SML focus measure is calculated at discrete increments of Δd. Due to this fact, maximum of the focus measure would result in a coarse estimate of depth for the object point (i, j). Application of a Gaussian fit to the focus measure values around the maximum will give a more precise result.

In the Gaussian fit, three focus measure values which are F_{m-1}, F_m and F_{m+1} are used. F_m is the maximum of the focus measure function calculated at $d = d_m$. F_{m-1} and F_{m+1} are calculated at d_{m-1} and d_{m+1}, respectively. Depth estimate from Gaussian interpolation is obtained using the following equation [20]:

$$df = \frac{(\ln F_m - \ln F_{m+1})(d_m^2 - d_{m-1}^2)}{2\Delta d[(\ln F_m - \ln F_{m-1}) + (\ln F_m - \ln F_{m+1})]}$$

$$-\frac{(\ln F_m - \ln F_{m-1})(d_m^2 - d_{m+1}^2)}{2\Delta d[(\ln F_m - \ln F_{m-1}) + (\ln F_m - \ln F_{m+1})]} \tag{3.13}$$

C. Error Correction

Due to the noise and other effects, the range image resulting from SFF procedure is error prone. In order to eliminate these errors, a postprocessing step on the image is necessary. The method in [22] is followed to do error correction. The procedure is conducted on range image pixel $R(i,j)$ according to the following rule

$$R(i,j) = \left\{ \; median(R(i,j)) \quad \text{if } df(i,j) \in [median(R(i,j)) \pm \delta * stdev_M(R(i,j))] \right.$$

(3.14)

where $median(R(i,j))$ is median filter response at the pixel (i,j) and $stdev_M(R(i,j))$ is standard deviation calculated in a $M \times M$ window around the pixel (i,j). δ is the smoothing parameter.

3.2 Visual Classification

Visual classification is applied on 3D reconstruction from focus, which is in the form of a range image. In this stage, a curvature-based segmentation method is applied on the piecewise-smooth surface function of a microscopic object [28]. This segmentation enables us to learn whether a surface patch of the range image is planar, cylindric, elliptic or hyperbolic. In addition to that visual classification is very important for object recognition. Objects with different geometries, as shown in Fig. 3.3, can be classified according to their curvatures.
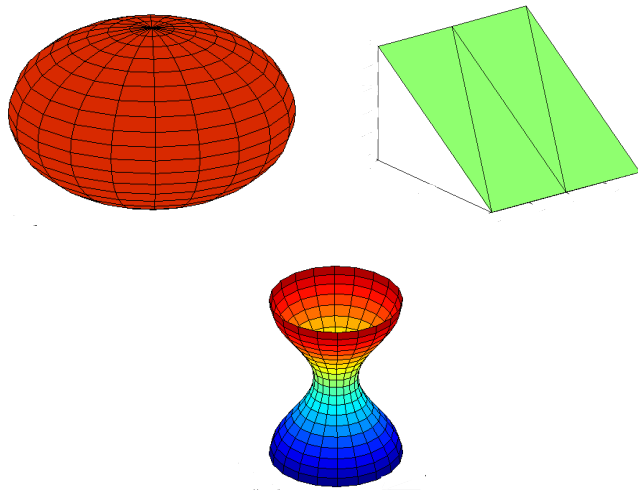

Figure 3.3: Objects with Different Surface Curvatures

3.2.1 HK Segmentation of Range Images

The result of SFF algorithm is in the form of a range image which has the same dimensions with the image of the object. In order to find shape composition of the visible surface of an object, a curvature-based segmentation has to be applied. HK segmentation, which partitions a range image into regions of homogeneous shape, is a proper method for this classification [29]. This method is based on differential geometry. According to differential geometry, local surface shape is uniquely determined using first and second derivatives. Gaussian and mean curvature combine these first and second derivatives to acquire scalar surface features that are invariant to rotations, translations and changes in parameterization. Hence, visible surfaces in range images have the same mean and Gaussian curvature from any viewpoint under orthographic projection [28].

There are eight fundamental surface types, shown in Fig. 3.4, that can be characterized using only the sign of the mean curvature (H) and Gaussian curvature (K) as shown in Table 3.1, where T is the surface label image.
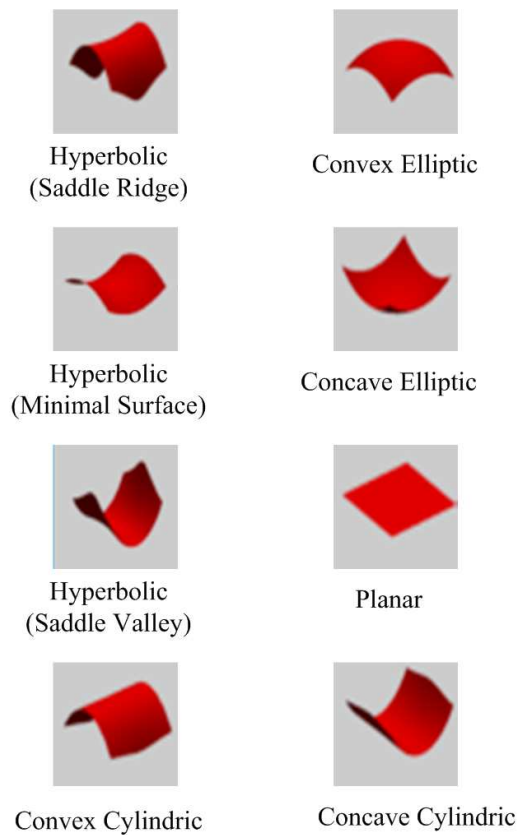

Hyperbolic (Saddle Ridge)   Convex Elliptic

Hyperbolic (Minimal Surface)   Concave Elliptic

Hyperbolic (Saddle Valley)   Planar

Convex Cylindric   Concave Cylindric

Figure 3.4: Eight fundamental surface types

Table 3.1: Shape Classification Scheme

	$K > 0$	$K = 0$	$K < 0$
$H < 0$	Convex Elliptic T = 1	Convex Cylindric T = 2	Hyperbolic (Saddle Ridge) T = 3
$H = 0$	none T = 4	Planar T = 5	Hyperbolic (Minimal Surface) T = 6
$H > 0$	Concave Elliptic T = 7	Concave Cylindric T = 8	Hyperbolic (Saddle Valley) T = 9

Gaussian and mean curvature can be calculated by convolving range images with first and second derivative window operators as in [28]. Due to the fact that second derivative operator amplifies high frequency noise in the images, which would degrade the quality of surface curvature estimation, a smoothing stage is necessary. A 7×7 binomial weight (approximately Gaussian) smoother is applied to the range image for smoothing. The binomial smoothing window can be written as $S = ss^T$ where s is given as

$$s = \frac{1}{64} \begin{bmatrix} 1 & 6 & 15 & 20 & 15 & 6 & 1 \end{bmatrix}^T \tag{3.15}$$

After the smoothing stage, 7×7 derivative operators can be applied to the range images. The operators are given as

$$D_x = d_0 d_1^T \ \ D_y = d_1 d_0^T \ \ D_{xx} = d_0 d_2^T \ \ D_{yy} = d_2 d_0^T \ \ D_{xy} = d_1 d_1^T \tag{3.16}$$

where column vectors d_0, d_1 and d_2 are as follows:

$$d_0 = \frac{1}{7} \begin{bmatrix} 1 & 1 & 1 & 1 & 1 & 1 & 1 \end{bmatrix}^T \tag{3.17}$$

$$d_1 = \frac{1}{28} \begin{bmatrix} -3 & -2 & -1 & 0 & 1 & 2 & 3 \end{bmatrix}^T \tag{3.18}$$

$$d_2 = \frac{1}{84} \begin{bmatrix} 5 & 0 & -3 & -4 & -3 & 0 & 5 \end{bmatrix}^T \tag{3.19}$$

Using (3.15)-(3.19), partial derivatives of the range images are calculated by the following 2-D image convolutions,

$$R_x(i, j) = D_x * S * R(i, j)$$

$$R_y(i, j) = D_y * S * R(i, j) \tag{3.20}$$

$$R_{xx}(i, j) = D_{xx} * S * R(i, j)$$

$$R_{yy}(i, j) = D_{yy} * S * R(i, j)$$

$$R_{xy}(i, j) = D_{xy} * S * R(i, j) \tag{3.21}$$

Mean(H) and Gaussian(K) images are obtained using (3.20)-(3.21) as follows:

$$H = \frac{(1 + R_x^2)R_{yy} - 2R_x R_y R_{xy} + (1 + R_y^2)R_{xx}}{2(1 + R_x^2 + R_y^2)^{3/2}} \tag{3.22}$$

$$K = \frac{R_{xx}R_{yy} - R_{xy}^2}{(1 + R_x^2 + R_y^2)^2} \tag{3.23}$$

In order to calculate surface curvature sign images $sgn_\varepsilon(H(i, j))$ and $sgn_\varepsilon(K(i, j))$, a signum function, with a zero threshold(ε) for H and K images, is employed according to the following rules,

$$sgn_\varepsilon(x) = \begin{cases} +1 & \text{if } x > \varepsilon \\ 0 & \text{if } |x| \leq \varepsilon \\ -1 & \text{if } x < -\varepsilon \end{cases} \tag{3.24}$$

Final stage of HK segmentation is to determine a surface label image $T(i, j)$ as mentioned in Table 3.1. This is accomplished by employing surface curvature sign images in the following formula:

$$T(i, j) = 1 + 3(1 + sgn_\varepsilon(H(i, j))) +$$

$$(1 - sgn_\varepsilon(K(i, j))) \tag{3.25}$$

Using the image $T(i, j)$, the range image $R(i, j)$ is partitioned to regions of homogeneous shape, and surface structure of the microscopic object is obtained.

Chapter 4

Mechanical Characterization

Mechanical property characterization of a cell or embryo chorion is to extract elastic modulus information using cell boundary deformation. Mechanical characterization can be useful in diagnosis of cells and embryo, some samples of which are shown in Fig. 4.1-4.2. Elastic modulus information can be used to learn whether the cell is infected or not. In addition to that in an embryo microinjection experiment, it is very important to have a knowledge about mechanical characteristics of the embryo since it will ensure that extreme forces, which can harm the embryo, are not applied during indentation to the embryo by a manipulator. In this chapter, especially mechanical characterization of zebrafish embryo chorion is examined. Elastic mod-
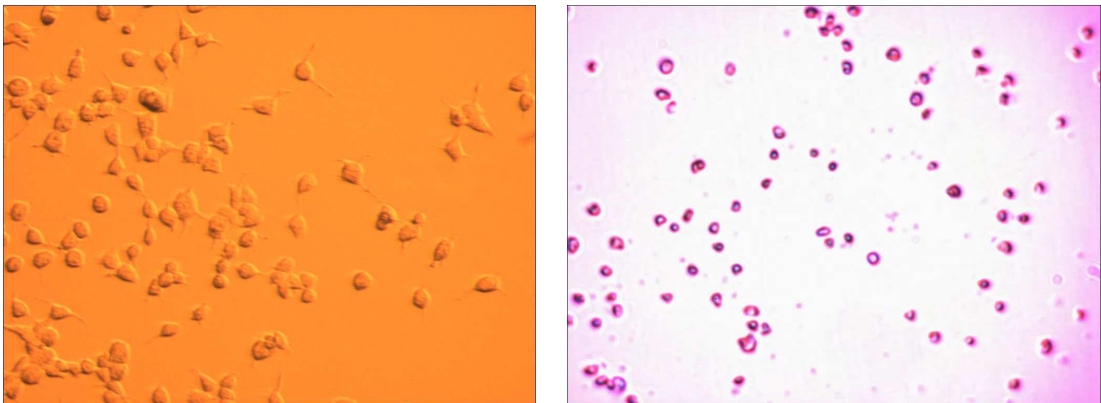

Figure 4.1: Cell samples: 293T Human Kidney Cell and Jurkat Cancer Cell

ulus describes embryo chorion's tendency to be deformed elastically when a force is applied to it. In the literature, there are several approaches for characterization of embryo chorion(biomembrane). These are contact mechanics models [32]- [33], micropipette aspiration model [34], and biomembrane point-load model [35]. The contact mechanics models treat a deformed object as a solid body and assumes small
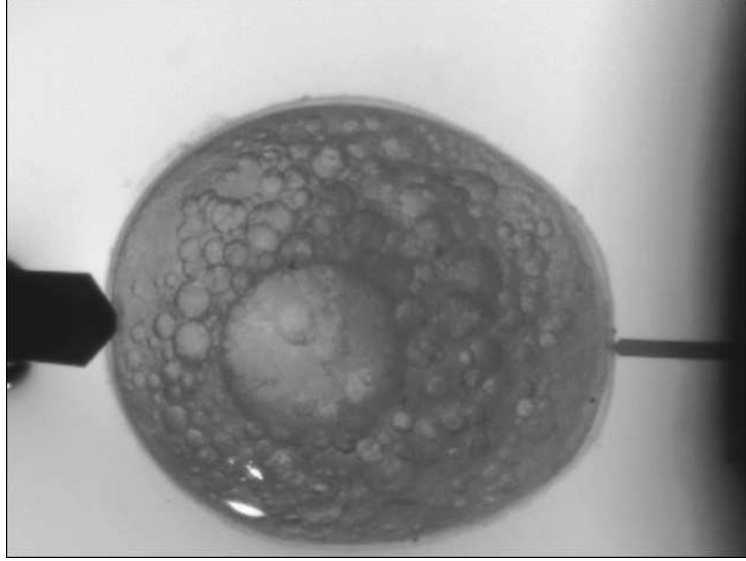
Figure 4.2: Zebrafish Embryo

deformation. Also, it is assumed that there is only a local dimple geometry change and the global geometry of the deformed object remains unchanged. However, these assumptions are not appropriate for mechanical characterization of zebrafish embryo chorion. Another approach for characterization is the micropipette aspiration technique. According to this model, a sucking pressure is applied on the biomembrane and biomembrane is elongated in the micropipette while biomembranes are indented by an AFM probe in experiments on the zebrafish embryo. On the other hand, the biomembrane point-load model is more appropriate for the experiments using AFM probe to indent biomembrane since it considers a biomembrane as a thin film and assumes that the inner cytoplasm provides a hydrostatic pressure on the membrane. Sun et.al [35] used micropipette instead of AFM probe to indent embryo chorion in their experiments.

4.1 Biomembrane Point-Load Model

In biomembrane point-load model, the biomembrane is deformed by an indenter and the membrane shape can be defined by three parameters a, w_d, and R as shown in Fig. 4.3. This model precisely estimates mechanical properties of zebrafish embryo chorion. The assumptions of the model are as follows:

1) The biomembrane encapsulates liquid that exerts a uniform hydrostatic pressure on the biomembrane.

26

2) The cell volume does not change.

3) The biomembrane has a negligible flexural rigidity, so that deformation is caused by membrane stretching alone.

4) The biomembrane is linearly elastic.

5) The cell is free of initial membrane stress or residual stress.

6) The model starts with a planar circular area with zero residual stress.

An AFM probe of width $2c$ exerts a force F on the biomembrane, creating a dimple with radius a and depth w_d and semicircular curved surfaces with radius R. The model is a good approximation for the shape composition of membrane after indentation.
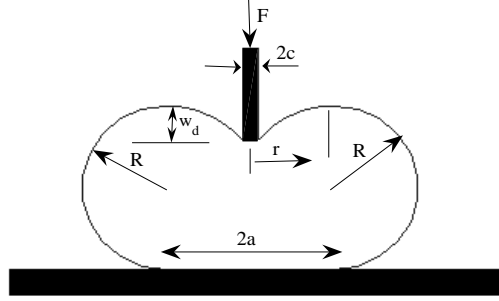

Figure 4.3: Deformation of an Embryo Membrane by an Indenter

In the model, first the force equilibrium at the local dimple is considered. As shown in Fig. 4.3, the internal pressure produces a force $\pi r^2 p$ counterbalancing the applied force F, where p is the internal pressure. Also, due to the membrane stress σ_d, there is another counterbalancing force $\sigma_d sin\,\theta 2\pi rh$. A small angle approximation, which assumes that $dw/dr \approx sin\theta \approx \theta$, where w is the deformed dimple profile [37], is used. Thus, the force balance equation at the equilibrium is formed as follows:

$$F = \pi r^2 p + \sigma_d sin\,\theta 2\pi rh \qquad (4.1)$$

where h is membrane thickness.

Integrating (4.1) with a boundary condition of $w = 0$ at $r = a$ and approximating $p = F/(\pi a^2)$ yields the following dimple profile

$$w = -\frac{F}{4\pi\sigma_d h}\left[1 - \left(\frac{r}{a}\right)^2 + \ln\left(\frac{r}{a}\right)^2\right] \qquad (4.2)$$

27

which is valid in $c \leq r \leq a$. The dimple depth from the maximum height of the deformed membrane, as shown in Fig. 4.3, can be calculated by evaluating (4.2) at $r = c$ as:

$$w_d = w|_{r=c} = -\frac{F}{4\pi\sigma_d h}\left[1 - \left(\frac{c}{a}\right)^2 + \ln\left(\frac{c}{a}\right)^2\right] \tag{4.3}$$

Within the dimple, each ring element on the membrane of radius r and width dr is stretched by the external load to a final width of $dr/\cos\theta$. So, elastic strain, ε_d, on such an element is given by

$$\varepsilon_d = \frac{\frac{dr}{\cos\theta} - dr}{dr}$$

$$\approx \frac{\theta^2}{2}$$

$$= \frac{1}{2}\left(\frac{dw}{dr}\right)^2 \tag{4.4}$$

Due to the fact that elastic strain on a membrane is proportional to area change [37], second-order terms can be ignored, and the average strain on the biomembrane can be given as

$$\overline{\varepsilon}_d = \frac{1}{2}\frac{\int_c^a \frac{1}{2}\left(\frac{dw}{dr}\right)^2 r\,dr}{\int_c^a r\,dr} \tag{4.5}$$

where denominator is the area of the annulus, with c and a the inner and outer radii, respectively.

According to linear elasticity [38]- [39],

$$\bar{\sigma}_d = \frac{E}{1 - \nu}\overline{\varepsilon}_d \tag{4.6}$$

where E is the biomembrane elastic modulus and ν is the Poisson ratio.

Combination of (4.5) and (4.6) yields the force equation for zebrafish embryo chorion

$$F = \frac{2\pi E h w_d^3}{a^2(1 - \nu)}\left[\frac{3 - 4\zeta^2 + \zeta^4 + 2\ln\zeta^2}{(1 - \zeta^2)(1 - \zeta^2 + \ln\zeta^2)^3}\right] \tag{4.7}$$

where $\zeta = c/a$. Due to the fact that in the experiments instead of a holding pipette, a force sensing probe is used to hold the zebrafish embryo, the measurements of the parameter a were conducted from the dimple side as done in [35].

Chapter 5

Experimental Results and Discussion

In this chapter, experimental results for optical system calibration, micropositioning and trajectory following tasks, visual reconstruction and classification, and mechanical characterization of zebrafish embryo are given. Initially, microassembly workstation in which the experiments were conducted is introduced.

5.1 Hardware Setup

The experiments were conducted on the microassembly workstation shown in Fig. 5.1. There are two manipulation stages and each of them consists of three PI M-111.1 high-resolution micro-translation stages to give motion to the probe/gripper with 50 nm incremental motion in x, y and z positioning axes. Also, there is a sample stage which consists of two PI M-111.1 high-resolution micro-translation stages which gives motion in x and y positioning axes. In the visual servoing experiments, a Zyvex microgripper with a 100 μm opening gap was used at the manipulation stages. Then, in the mechanical characterization experiments a Nanosensors TL-CONT AFM probe and a Femtotools force sensing probe were employed to manipulate zebrafish embryo. Manipulation and sample stages are controlled by a dSpace ds1005 motion control board. In order to avoid problems related to vibration in micromanipulation, a Table Stable TS-140 isolation table is used.

Nikon SMZ 1500 stereomicroscope coupled with a Basler A602fc and a Sony XCD-X710CR camera, orthogonal to XY plane with 9.9 $\mu m \times$ 9.9 μm and 4.65 $\mu m \times$ 4.65 μm cell sizes, respectively, are utilized to provide visual feedback. The microscope has 1.2X and 1.6X objectives, and additional zoom. Additional zoom can be varied between $0.75X - 11.25X$, implying $15 : 1$ zoom ratio. In addition to these
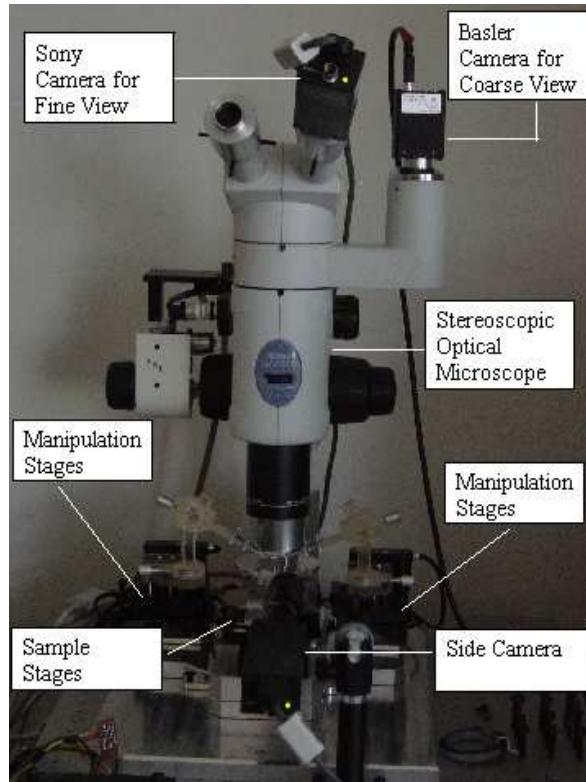
Figure 5.1: Microassembly Workstation

cameras, there is also a side camera which is a Sony XCD-X710CR. The side camera is positioned using an Edmund Optics articulating arm. Two calibration patterns, Edmund Optics IAM-1 with 50 μm and 200 μm square sizes, and Mvtec calibration grid with 70 μm radius circles (Fig. 5.2) were employed to calibrate the optical system.
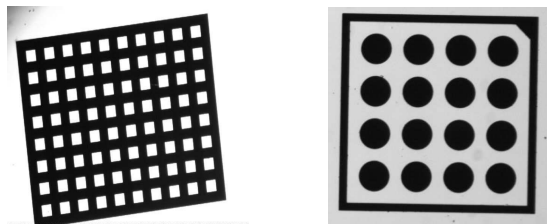

Figure 5.2: Square and Circular Calibration Patterns

5.2 Calibration Results

Before visual servoing tasks were performed, a sub-micron accurate calibration of the optical system was accomplished through a parametric model [16]. Two different

types of calibration patterns were used to establish the correspondence between the world and image coordinates under 1X and 4X zoom levels, hence implying ~ 1.6 and ~ 6.4 magnifications as can be verified from Table 5.1. For the square one, a Sobel edge operator, edge linking and then a line fitting algorithm were applied to obtain every edge line of the squares. Corners of the squares -intersections of the calculated edge lines- were taken as the calibration points. For the round calibration grid, the center coordinates of the circles were calculated through a least square solution. Calibration results are tabulated in Table 5.1.

It can be observed from this table that the radial distortion coefficient is very small. This proves that the microscope lenses are machined very precisely. Moreover, β and γ angles have non-zero values which can be resulted from a mechanical tilt of the microscope stage or from an inaccurate design of the calibration pattern.

In the experiments it was observed that the circle grids give more accurate calibration results. Due to imperfect illumination, lens aberration, systematic and random sensor errors, the image might be blurred by a point spread function (PSF) and the features might not be extracted very accurately. Flusser and Zitova [18] claim that most of the PSF are circularly symmetric and circular shapes are invariant to this type of PSF. Thus, our experimental results are in accordance with their interpretation as shown in Table 5.2.

5.3 Real-Time Feature Tracking

Visual servoing algorithms necessitate real-time measurement of the image features in an efficient, accurate and robust manner. Both Kalman filtering and the efficient second-order minimization (ESM) algorithm [19], which is based on the minimization of the sum-of-squared-differences (SSD) between the reference template and the current image using parametric models, were employed in our experiments. The ESM algorithm has high convergence rate like the Newton method, however, it can track more frames per second than the other tracking algorithms. The ESM algorithm accomplished to track a 50×50 window up to 250 pixels/sec velocity at 33 Hz in the experiments.

Table 5.1: Computed Intrinsic and Extrinsic Parameters using Circular and Square Patterns

	Circular		Square	
	1X	4X	1X	4X
M	1.5893	6.3859	1.6236	6.444
T_{op} (μm)	200490	200610	199690	200880
f (μm)	126150	31415	122990	31174
d (μm)	78750	4955.5	75441	4833.5
κ (μm^{-2})	$-8.4e-10$	$1.5e-11$	$2.1e-10$	$1.5e-10$
α (deg)	90.7144	88.9825	87.2897	95.4143
β (deg)	-2.7912	2.6331	-1.6248	-1.9407
γ (deg)	175.9179	0.9088	177.6637	178.2925
T_x (μm)	-781.4	76.755	-1792.7	-1653.1
T_y (μm)	-55.002	-156.58	-1210.3	-1194.5
T_z (μm)	204900	36370	198430	203610

Table 5.2: 3D Reprojection Errors of Circular and Square Patterns for 1X and 4X

	Circular		Square	
	1X	4X	1X	4X
Mean Error (μm)	0.2202	0.0639	0.4618	0.0920
Standard Deviation (μm)	0.3869	0.1321	2.9101	0.5316
Maximum Error (μm)	1.7203	0.5843	12.0898	2.3988

5.4 Visual Servoing Results

In the experiments, micropositioning and trajectory following tasks were performed at 1X and 4X zoom levels using calibrated visual servoing (VS) algorithm. The control input is designed according to (2.28). Real-time feature tracking is employed to track the opening of the Zyvex microgripper shown in Fig. 5.3 and mean of square corner points is used as $f(k)$ in VS. For the optimal control design, Q and L matrices in (2.28) were chosen as diagonal matrices with diagonal entries (0.9,0.9) and (0.025,
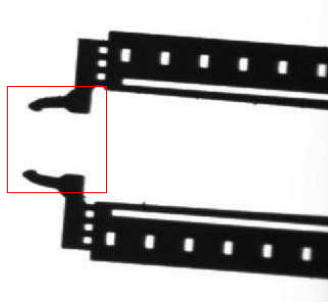
0.05) respectively.

Figure 5.3: Real-time tracking of microgripper opening

Micropositioning VS results are plotted in Fig. 5.4-5.5. In this task, a reference of 50 pixels in x and y directions is given to the manipulator. The distance from initial position to the reference position for 1X and 4X zoom levels is $311\mu m$ and $77\mu m$, respectively. As shown in Fig. 5.4-5.5, control effort (velocity) is constant due to the saturation limit at the beginning. Decrease in the error results in decrease of the velocity and it can be recognized when velocity input to the micro-translational stage is less than the saturation limit. Performance parameters of VS in micropositioning, which are settling time(t_s), accuracy and precision, are tabulated in Table 5.3. Settling time is less than 1 second for both zoom levels. Tasks are achieved with an accuracy of $9.86\mu m$ and $1.35\mu m$ for 1X and 4X, respectively, which implies an error of less than 3% at the settling time. Also, the precision is very low which is due to the robustness of calibrated VS.

Table 5.3: Results of micropositioning for calibrated visual servoing

	Step (pixels)	t_s (sec)	Acc. (μm)	Prec. (μm)
$1x$	50	0.80	9.86	2.71
$4x$	50	0.45	1.35	0.57

The trajectory following results for circular, square and sinusoidal trajectories are depicted in Figs. 5.6-5.8. Tracking performance parameters for different trajectories are presented in Table 5.4. Due to the fact that effective pixel size for 1X and 4X zoom levels are $6.23\mu m$ and $1.55\mu m$, respectively, accuracies for both cases in terms
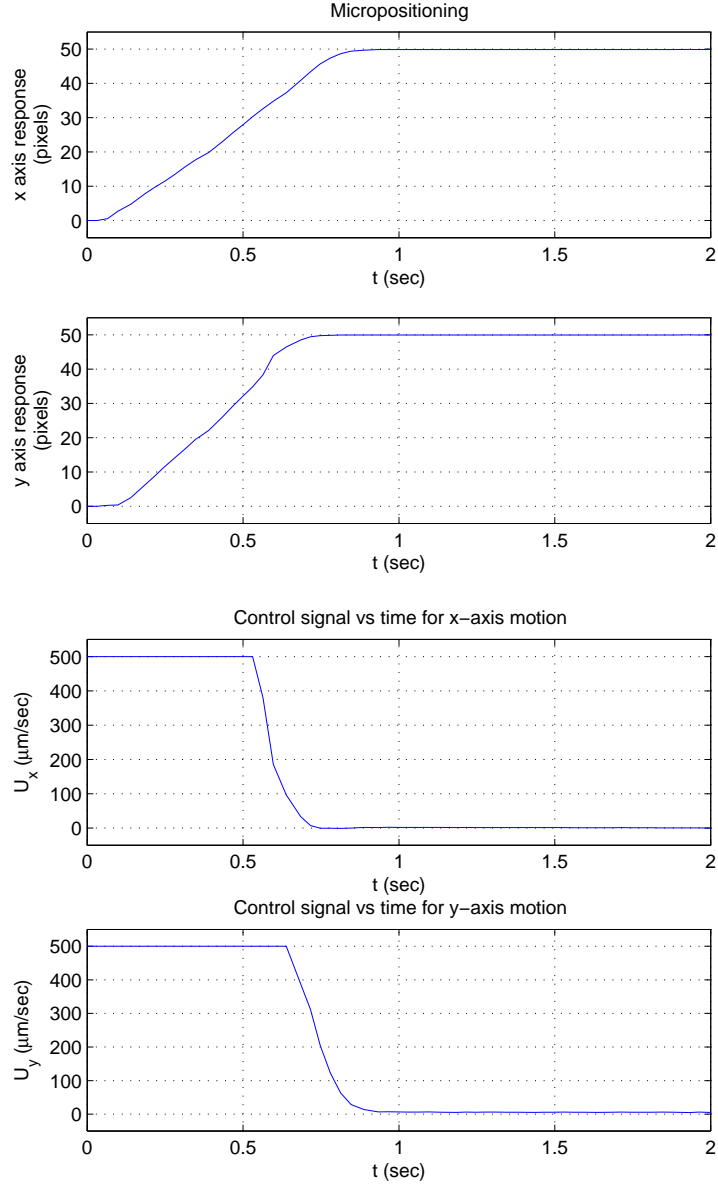
33

Figure 5.4: Step responses and control signals of calibrated VS at 1X

of pixels in different trajectory following tasks is nearly the same. The results show that desired trajectories are tracked accurately in general.

5.5   Visual Reconstruction and Classification Results

In this section, first the application of SFF algorithm on synthetic and real data is presented, and then surface shape classification results of the range images, acquired
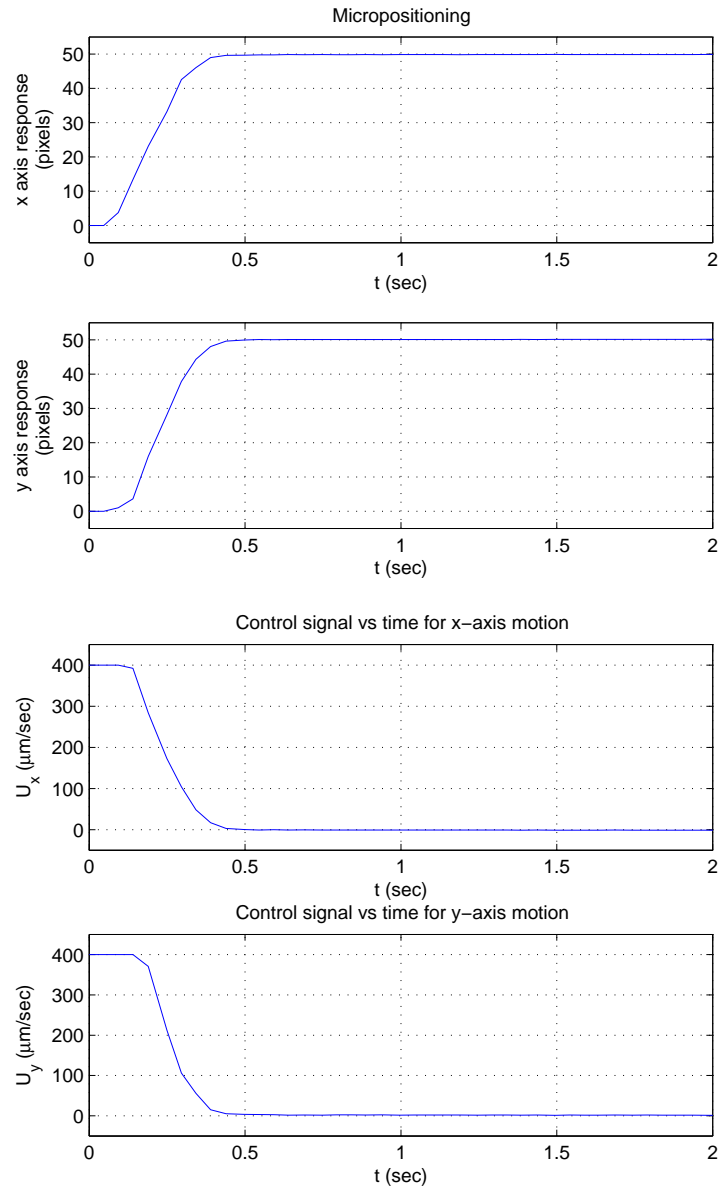
Figure 5.5: Step responses and control signals of calibrated VS at 4X

Table 5.4: Results of trajectory tracking for calibrated visual servoing

	Square		Circular		Sinusoidal	
	Acc.	Prec.	Acc.	Prec.	Acc.	Prec.
	(μm)	(μm)	(μm)	(μm)	(μm)	(μm)
$1x$	5.93	2.28	7.72	1.40	4.79	2.37
$4x$	1.47	1.19	1.57	0.95	1.12	1.31
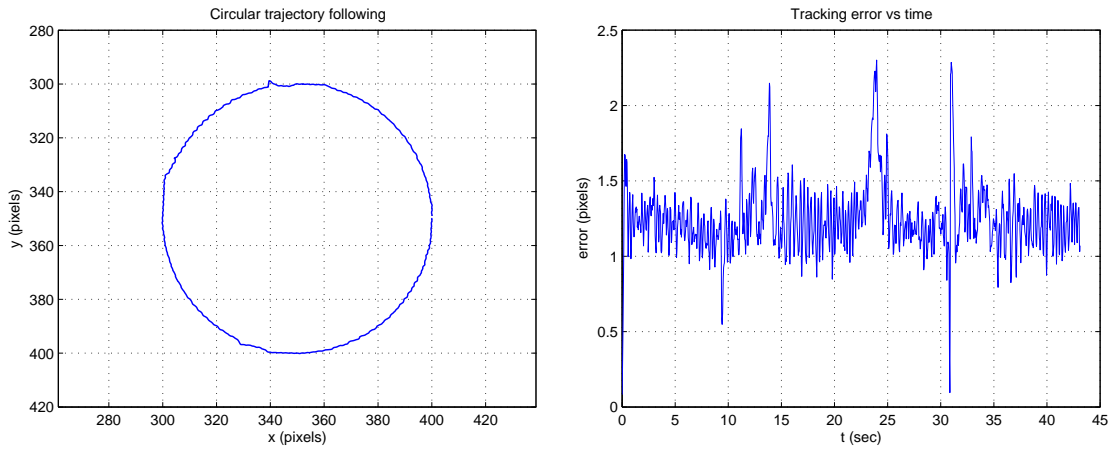
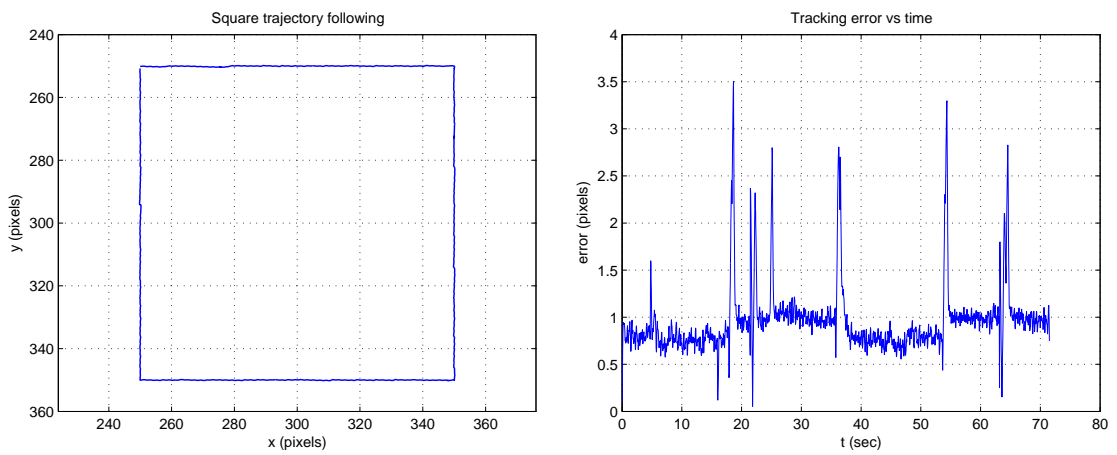Figure 5.6: Circular trajectory and tracking error in calibrated VS at 1X

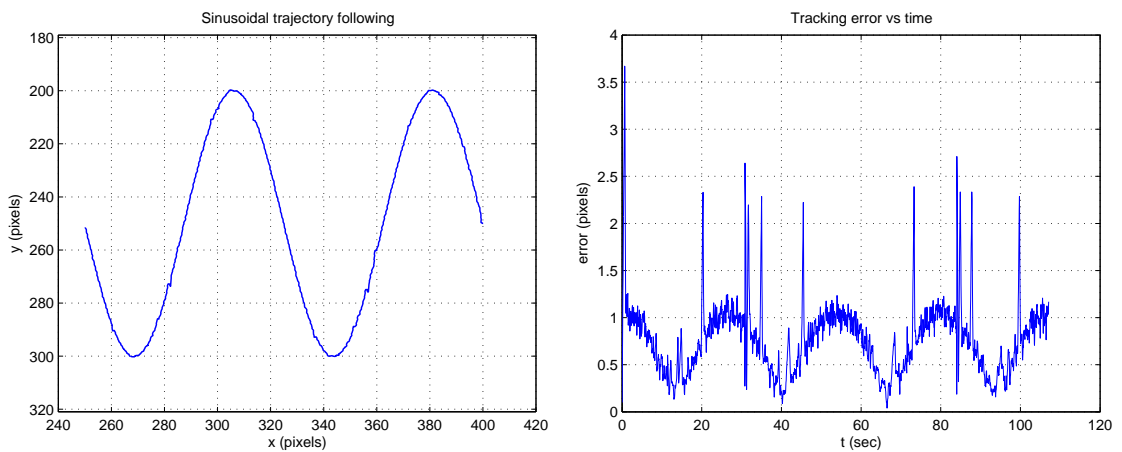Figure 5.7: Square trajectory and tracking error in calibrated VS at 1X

Figure 5.8: Sinusoidal trajectory and tracking error in calibrated VS at 1X

from the application of SFF algorithm, using HK segmentation is given.

5.5.1 SFF Results

SFF is first evaluated on a synthetic texture image shown in Fig. 5.9(a). An image sequence is created in which at each focus level a different part of the parabolic object is focused. In the creation of these images, camera defocus PSF was modeled as a 2-D Gaussian function and given by $(1)/(2\pi\sigma^2)exp(-(i^2+j^2)/(2\sigma^2))$ where σ is the deviation of the Gaussian function [27]. A 7×7 2-D Gaussian filter with $\sigma = 1$ is employed to create defocus effect on the textured image.

SFF algorithm is applied on the image sequence, some of which shown in Fig. 5.9(b), (c), (d), corresponding to a parabolic shape created assuming $\Delta d = 25\mu m$ and object height is $500\mu m$. The resulting focused image is shown in Fig. 5.9(e).

Since the spikes in range image would result in problems at HK segmentation stage, these were detected and replaced with the response of median filtering according to (3.14). In this error correction procedure, median filtering and standard deviation calculation are done in a 9×9 window, and smoothing parameter $\delta = 2$. After this procedure, also, a 7×7 averaging filter is applied to further smoothen the image. Resulting range image is shown in Fig. 5.10.

After the application of SFF on synthetic data, it is also evaluated on real data. The image sequence shown in Fig. 5.11(a)-(c), which belongs to a solder ball on paper, is captured under an optical microscope. Initially as it is shown in Fig. 5.11(a), paper in the background is focused. Then, micro-translational stage is moved with a $\Delta d = 50\mu m$ until whole object is scanned (Fig. 5.11(b), (c)). The implementation of SFF on this image sequence resulted in the following focused image shown in Fig. 5.11(d). Error correction is also applied to the range image acquired from real data. However, due to the rough surface of the ball, the range image result is not very smooth (Fig. 5.12). Since the object is observed from above, only half of it can be examined. This is why lower part of 3-D map of the object is cylindric and the top part is spherical.

5.5.2 HK Segmentation Results

HK segmentation is initially applied on the parabolic profile, resulting from the application of SFF on synthetic data, to examine the surface structure of the synthetic object. Before the segmentation procedure, binomial smoothing window is
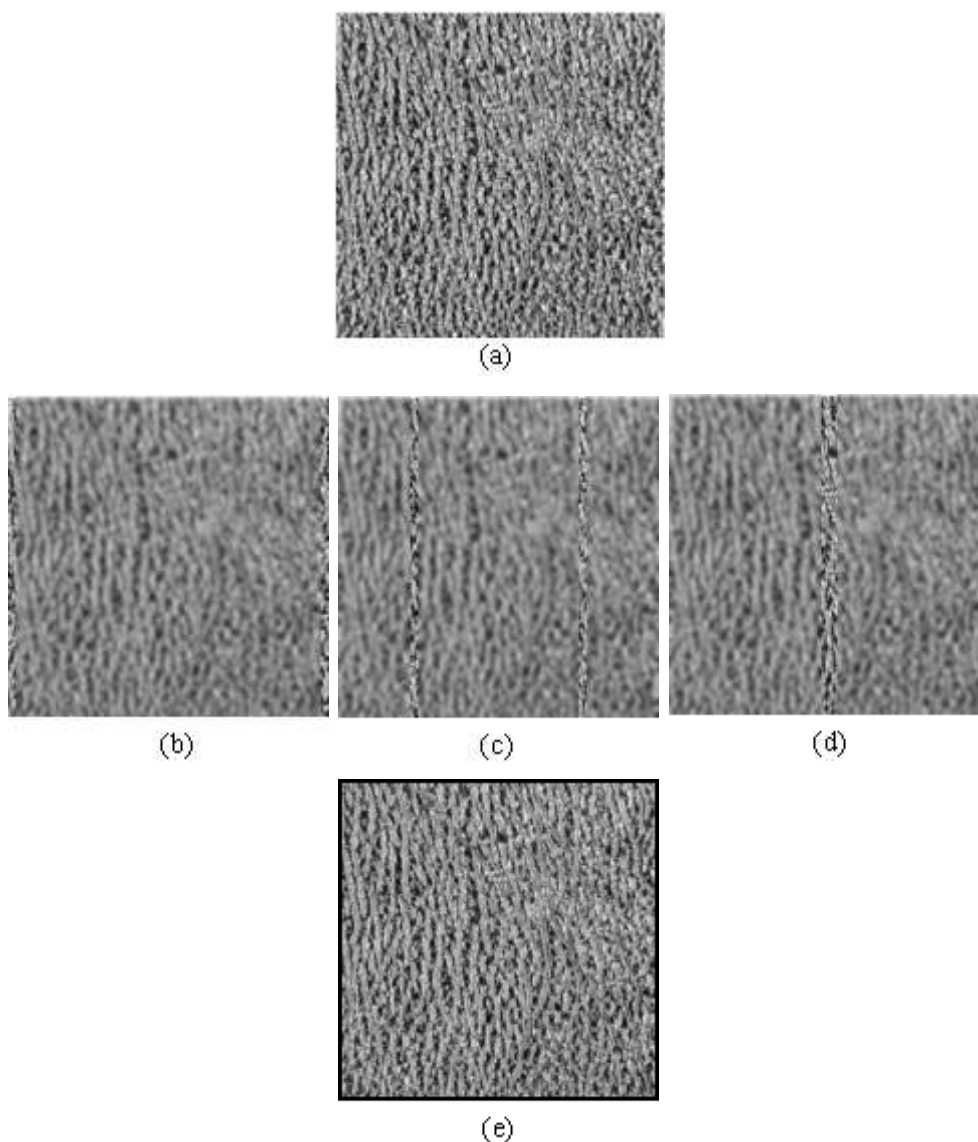
Figure 5.9: (a) Original Textured Image (b), (c), (d): Defocused Images in the Image Sequence for SFF (e) Resulting Focused Image from SFF

convolved with the range image. Also zero threshold ε for H and K images were determined as 0.03 and 0.015, respectively. In the resulting segmentation, as it is shown in Fig. 5.13, left and right of the maximum of the parabola is planar. The part of the range image near maximum of the parabola is mostly convex cylindric as expected. There are also some surface patches estimated as hyperbolic (saddle ridge) and convex elliptic. These patches are estimated that way due to the errors generated by SFF procedure, but the number of these patches is small and they are also convex. The edge of the surface is detected as concave cylindrical due to the fact that altitude of the edge points is 0. So, edges are estimated as a valley
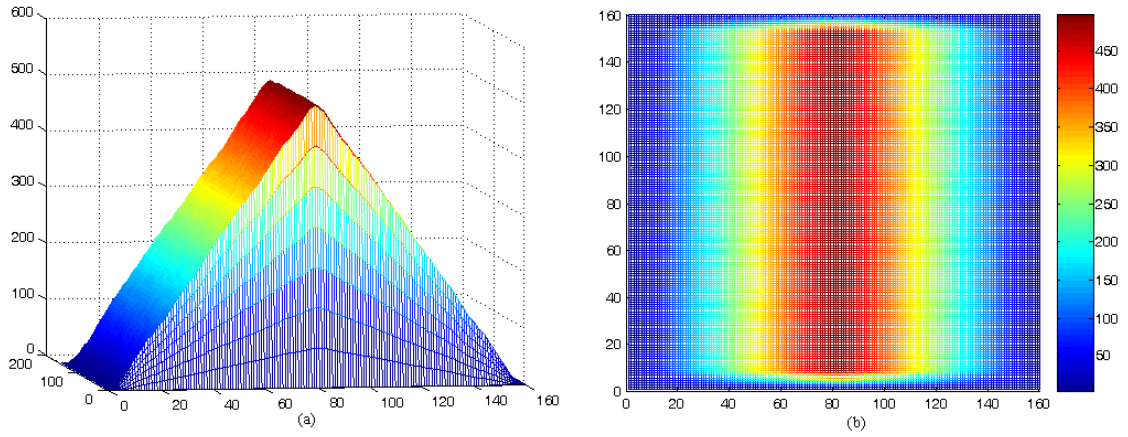
Figure 5.10: (a) Resulting Parabolic Range Image from Synthetic Data (b) Range Image x-y View
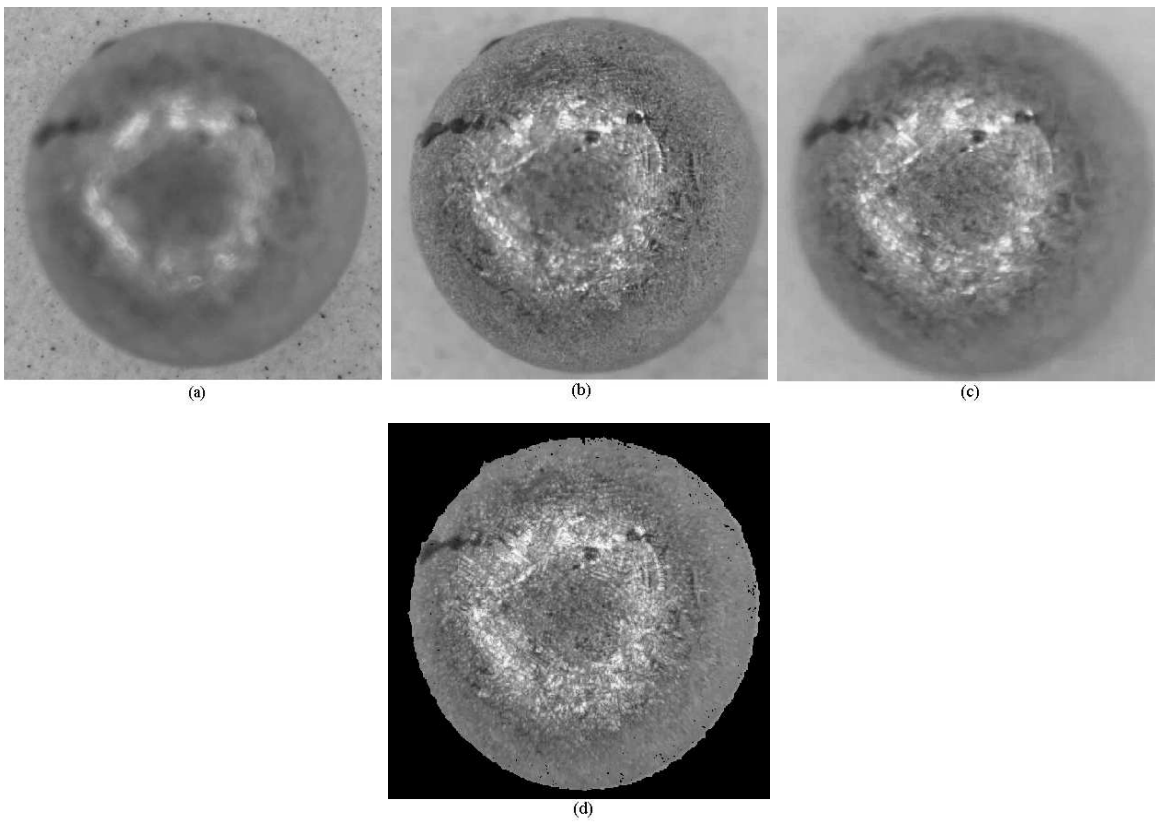

Figure 5.11: (a)-(c) Defocused Images of Solder Ball. (d) Resulting Focused Image from SFF.

compared to the planar surfaces at the sides.

HK segmentation is also evaluated on the 3D reconstruction result from real data. Binomial smoother is again convolved with the range image, and the same zero threshold values for H and K images are used. Then surface structure of the
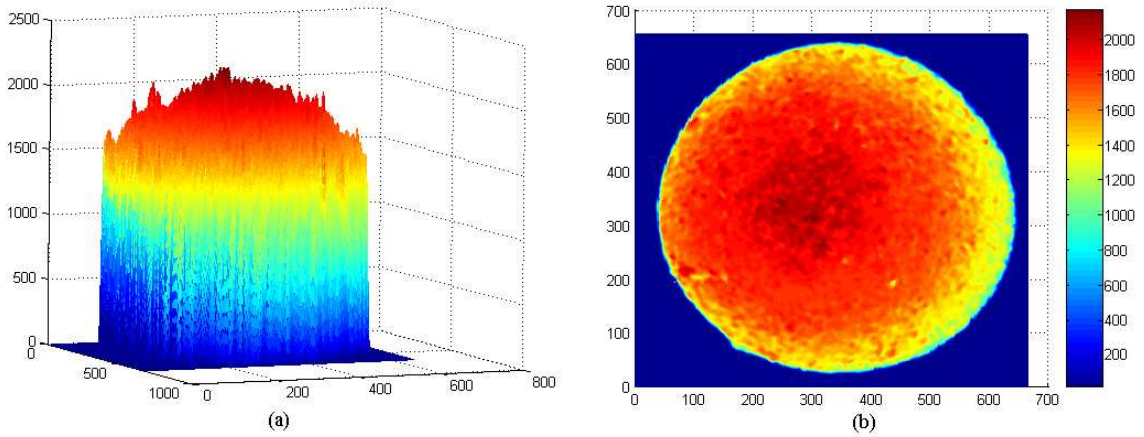
Figure 5.12: (a) Solder Ball Range Image (b) Range Image x-y View

solder ball was acquired by applying HK segmentation on the range image result of SFF as it is shown in Fig. 5.14. Due to the roughness of the ball surface, mostly concave and convex cylindric parts were detected on the upper surface of the object. There were also some hyperbolic patches again as a result of rough surface structure. Background of the object is estimated as planar due to the fact that object stands on a planar surface.

5.6 Mechanical Characterization Results

Zebrafish embryo chorion is mechanically characterized by employing a force sensing probe holding the embryo and sensing the generated forces during the cell is indented by an AFM probe, which are shown in Fig. 5.15. The image, which is captured when the measured force is maximum, used in the characterization is shown in Fig. 5.16. In order to characterize the embryo, boundary information of the embryo chorion has to be extracted.

The first step is to crop the dimple side of the embryo, shown in Fig. 5.17 (a), from where the measurements are acquired. Due to the fact that AFM probe in the scene acts as a disturbance in cell boundary extraction, it has to be segmented. To achieve that first the region including the probe is selected, then edge detection is applied and the region is filled with background gray level as shown in Fig. 5.17 (b). After segmenting the probe, Canny edge detection is applied on the image region including the segmented probe and embryo chorion to extract cell contour as shown
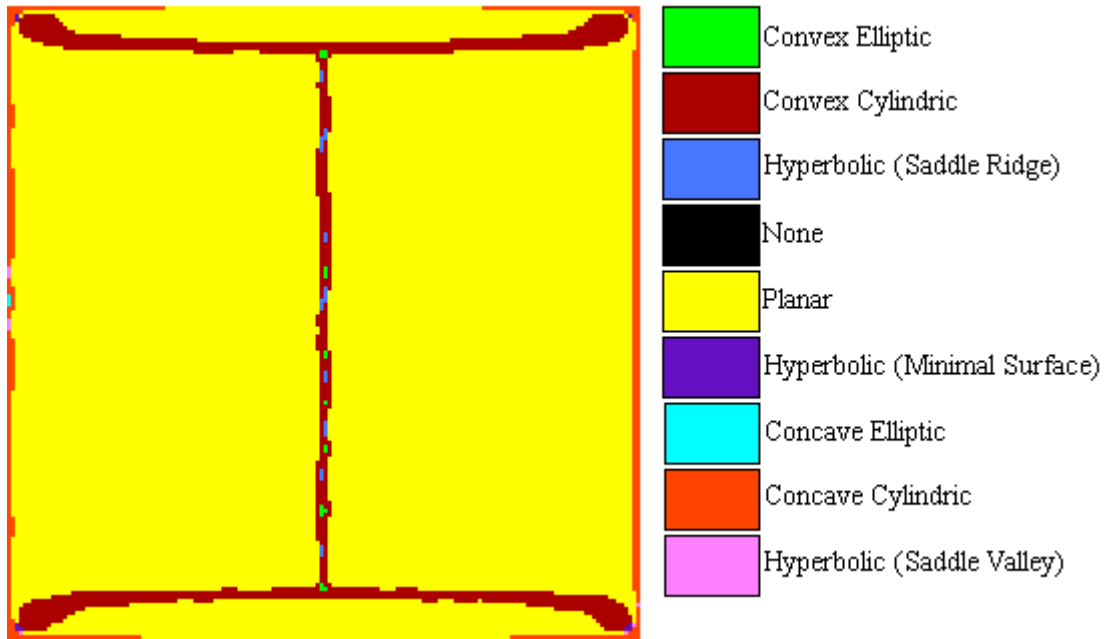
40

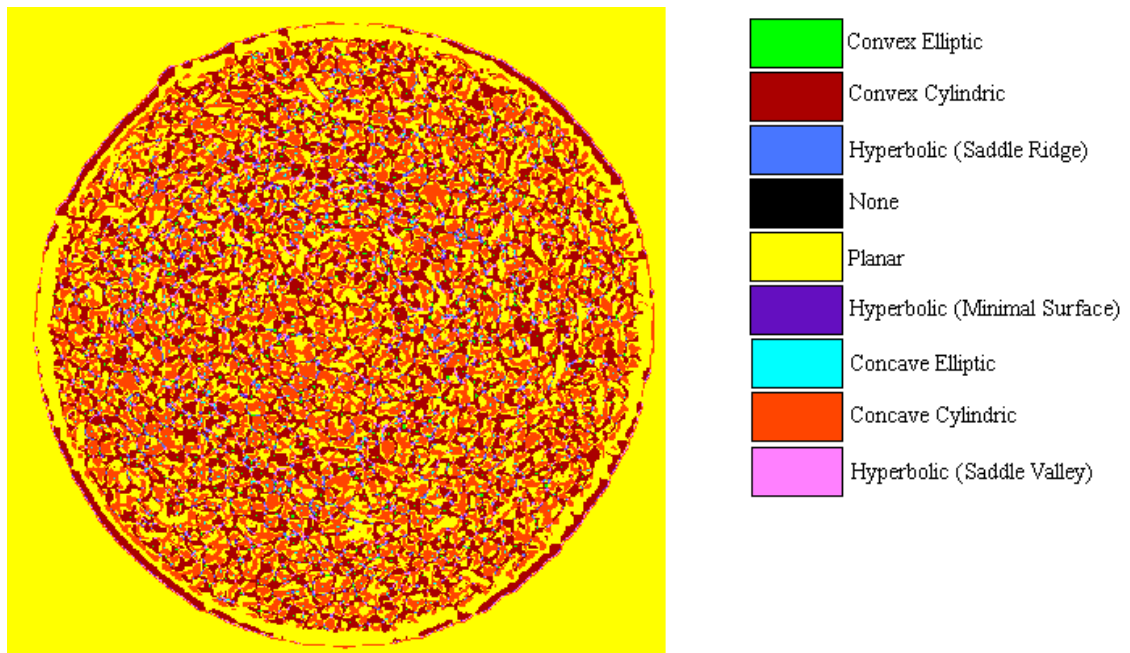Figure 5.13: HK Segmentation of Range Image Result of Synthetic Data

Figure 5.14: HK Segmentation of Range Image Result of Real Data

in Fig. 5.17 (c).

Cell contour information is fed into curve-fitting procedure to precisely estimate the parameters for mechanical characterization. First, cell contour data is taken as xfit vs. yfit with a weight on xfit points. Then, the data is smoothed using Loess(quadratic fit) with a span of 0.25. Resulting smoothed data is shown in Fig.
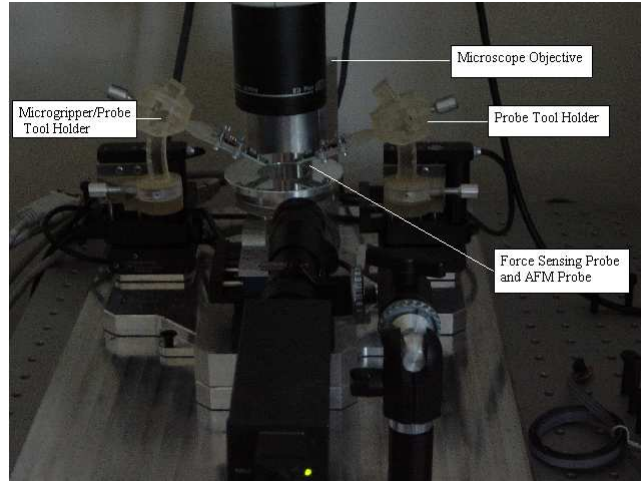
Figure 5.15: Force Sensing Probe and AFM Probe used in Cell Manipulation
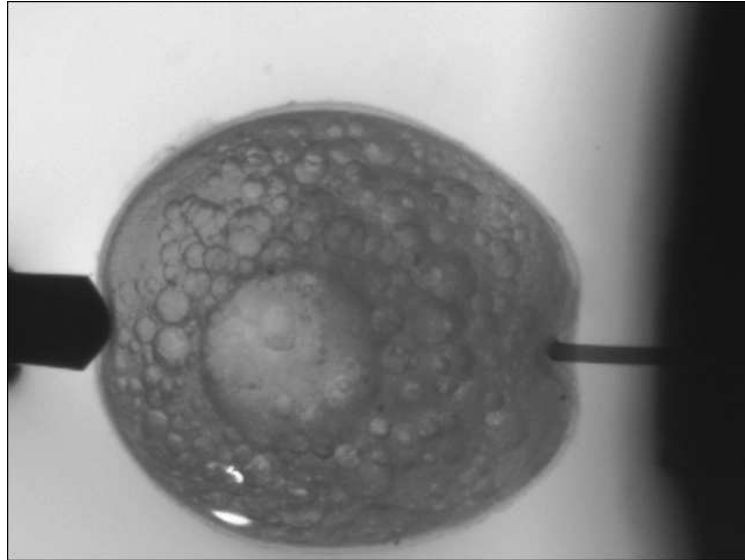
Figure 5.16: Zebrafish Embryo with Indenter and Force Sensing Probe

5.18.

After the smoothing stage, curve-fitting can be applied. Due to the fact that the curve is complex, eighth degree Gaussian fit using Trust-Region Reflective Newton algorithm is applied to cell boundary data. The curve fit shown in Fig. 5.18 is calculated using 1500 max number of iterations. The eighth degree Gaussian function used in the fit is as follows:

$$f_m(x) = a_1 e^{-((x-b_1)/c_1)^2} + a_2 e^{-((x-b_2)/c_2)^2} +$$

$$a_3 e^{-((x-b_3)/c_3)^2} + a_4 e^{-((x-b_4)/c_4)^2} +$$

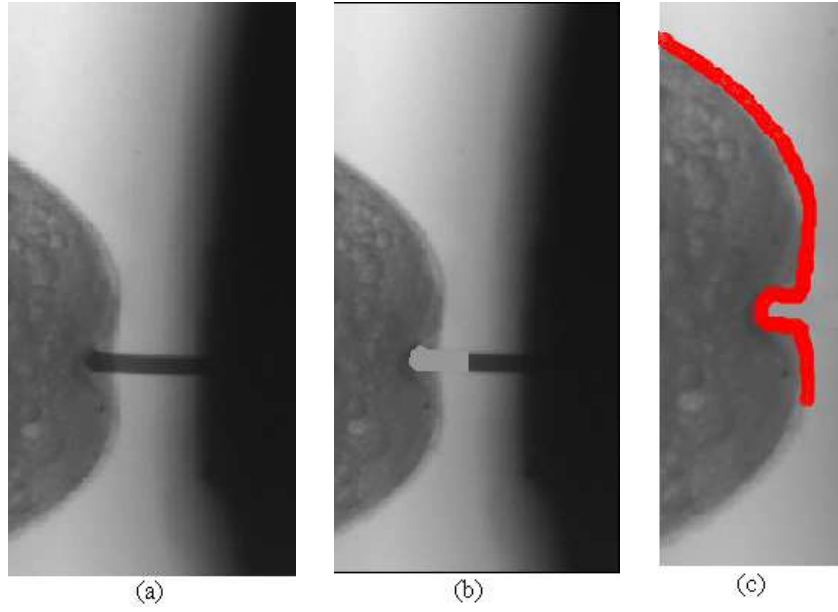Figure 5.17: (a) Dimple Side of Embryo Chorion (b) AFM Probe Segmentation (c) Extraction of Cell Boundary.
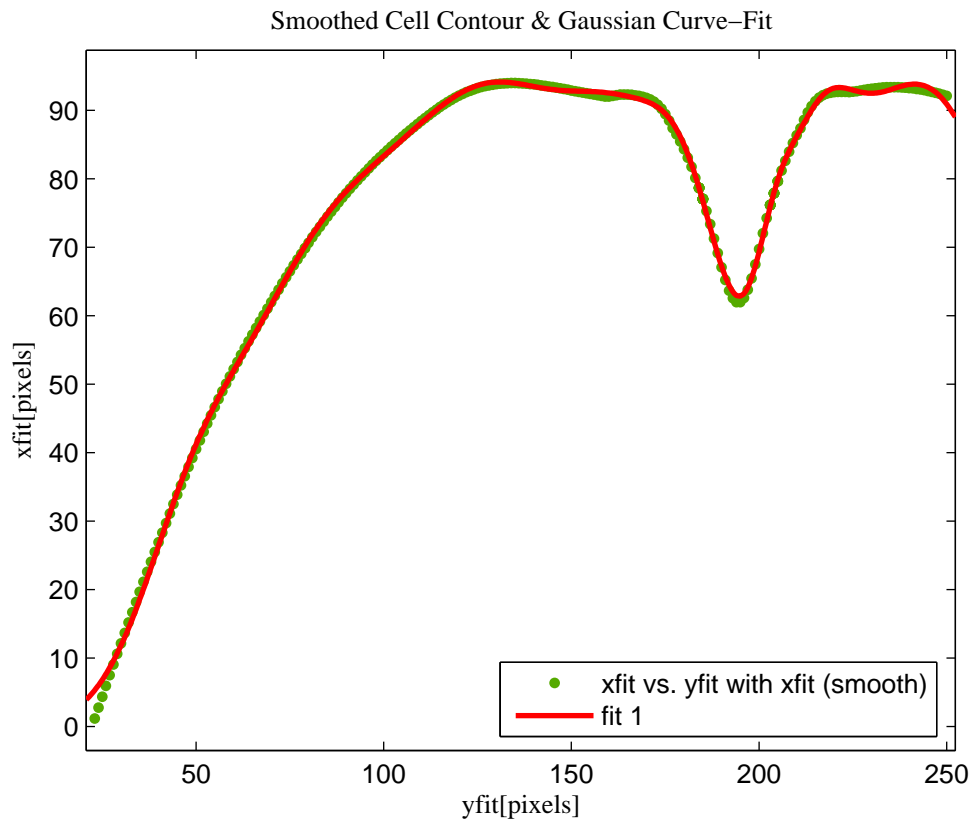

Figure 5.18: Smoothed Cell Contour and Gaussian Curve-Fit Result

$$a_5 e^{-((x-b_5)/c_5)^2} + a_6 e^{-((x-b_6)/c_6)^2} +$$

$$a_7 e^{-((x-b_7)/c_7)^2} + a_8 e^{-((x-b_8)/c_8)^2} \quad (5.1)$$

The parameter values resulting from the curve-fit are shown in Table 5.5. In the

Table 5.5: Coefficients of Gaussian Curve-Fit

Coefficient Number	a	b	c
1	89.38	129.5	44.25
2	93.14	243.3	41.71
3	9.011	203.7	6.922
4	28.6	213.3	14.61
5	44.78	77.2	30.84
6	17.99	182.5	13.58
7	40.7	169.9	23.55
8	17.26	48.01	18.9

cell boundary curve there are two local maximum and one global minimum. The parameters w_d and a, in elastic modulus equation which is given as follows:

$$E = \frac{Fa^2(1-\nu)}{2\pi h w_d^3} \left[\frac{(1-\zeta^2)(1-\zeta^2+\ln\zeta^2)^3}{3-4\zeta^2+\zeta^4+2\ln\zeta^2} \right] \tag{5.2}$$

can be evaluated using the local maximum at the left and the global minimum. The derivative of $f_m(x)$ is 0 at the local maximum coordinate $(x_1, y_1) = (130.98, 94.1202)$ and at the global minimum coordinate $(x_2, y_2) = (194.71, 62.8384)$. In order to calculate w_d and a in terms of metric coordinates, camera CCD cell size and microscope objective magnification information is used as follows:

$$w_d = |CS * (y_2 - y_1)/M|$$

$$a = |CS * (x_2 - x_1)/M| \tag{5.3}$$

where magnification $M = 1.2$ and cell size $CS = 4.65\mu m$. Resulting w_d and a are shown in Fig. 5.19. All the parameters used in elastic modulus calculation are tabulated in Table 5.6. The parameters h and ν are taken from [36], F is measured by force sensing probe and c parameter in ζ is half of the width of AFM probe.

The elastic modulus estimation procedure is also evaluated at different dimple depths and measured force configurations. Following mean elastic modulus and standard deviation results, which are tabulated in Table 5.7, are obtained.
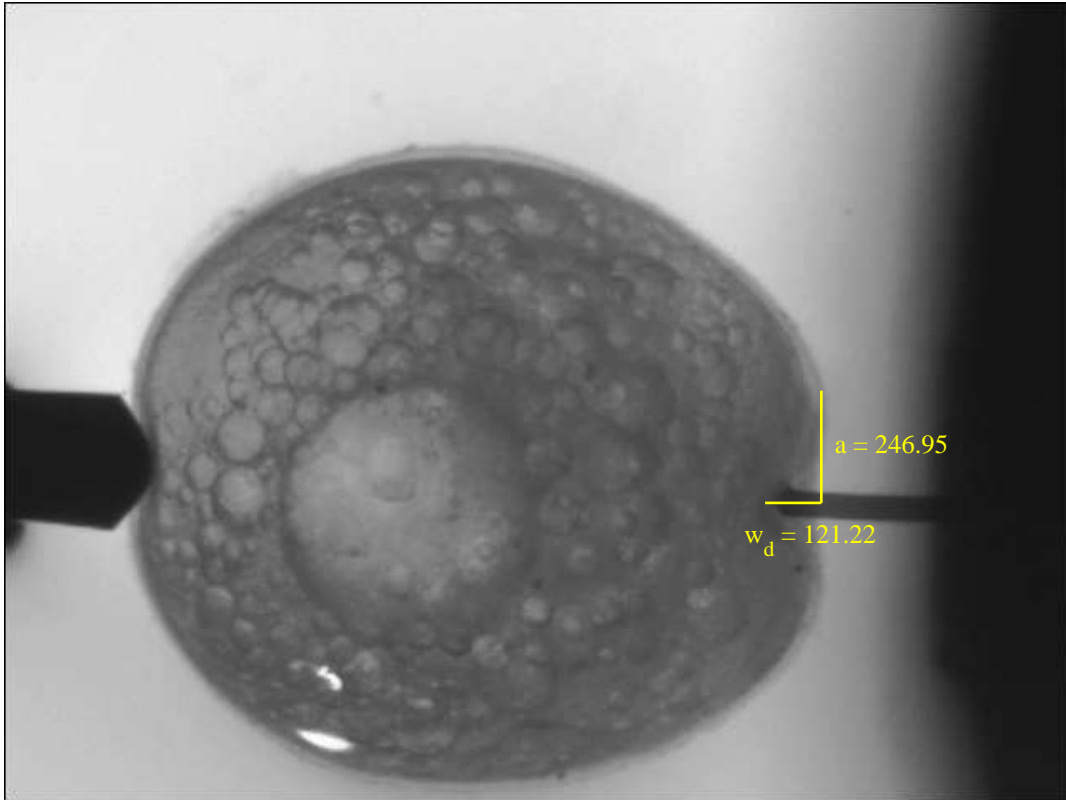
Figure 5.19: Geometric parameters w_d and a for mechanical characterization

Table 5.6: Parameter Values for Mechanical Characterization and Resulting Elastic Modulus

Parameter Name	Value in the Experiment
h (chorion thickness)	3 μm
w_d (dimple depth)	121.22 μm
a (dimple radius)	246.95 μm
ν (poisson ratio)	0.5
$\zeta(c/a)$	44.78
F (measured force)	197.24 μN
E (elastic modulus)	1.3237 MPa

Table 5.7: Elastic Modulus Evaluation Results at Different Dimple Depths

Mean Elastic Modulus	Standard Deviation
1.2791 MPa	0.05

The mean elastic modulus value implies that zebrafish embryo was at the gastrula stage during the experiment according to the results in [36]. Elastic modulus information can be used in automatic microinjection tasks and dynamic force estimation using cell boundary information.

Chapter 6

Conclusion

In this thesis, visual reconstruction and classification algorithms, and mechanical characterization are experimentally evaluated on microscopic samples. In addition to that results of experimental evaluation of calibrated image based visual servoing algorithm for various tasks in micro domain are presented.

More specifically, in Chapter 2 image-based visual servoing algorithms and optical system calibration algorithms are presented. In Chapter 3, a visual reconstruction from focus algorithm, SFF, and a visual classification algorithm, which is based on curvature-based segmentation, are outlined. The visual reconstruction algorithm uses 2D image sequence of a microscopic object captured at different focusing levels to create a 3D range image. Then, the visual classification algorithm takes the range image as an input and applies a curvature-based segmentation method, HK segmentation, which is based on differential geometry. The object is segmented into surface patches according to the curvature of its surface. In Chapter 4, a mechanical property characterization technique for cell and embryo is presented. In the characterization procedure, the biomembrane point-load model which extracts elastic modulus information from cell boundary deformation is given. In Chapter 5, first experimental results on optical system calibration and image-based visual servoing in micropositioning and trajectory following tasks are presented. Then, experimental results on visual reconstruction and classification of microscopic objects, and mechanical characterization of a zebrafish embryo using visual information are given.

Optical system calibration algorithm is evaluated at 1X and 4X zoom levels of the microscope and it was shown that the system is calibrated with sub-micron

reprojection error. Resulting intrinsic calibration parameters from this procedure were employed in image jacobian estimation. The image jacobian is used in vision-based control of the micromanipulators. Image-based visual servoing algorithm is employed in the control and it is shown that the algorithm works very precisely and accurately in the given tasks.

Then, it is shown that the visual reconstruction algorithm works successfully for synthetic and real image data. The range images are used to classify the surfaces of the objects according to their curvatures in the HK segmentation algorithm. For the synthetic data, range image is segmented into homogeneous surface patches. Due to the fact that the solder ball object has a rough surface, convex and concave surface patches are estimated from the range image.

Finally, a zebrafish embryo chorion is mechanically characterized using cell boundary deformation. Elastic modulus and developmental stage of the embryo are obtained successfully using visual information.

As a future work, real-time 3D reconstruction of the micromanipulation environment can be done. HK segmentation can be used for object recognition in a microassembly task if range images are obtained. Also, dynamic estimation of the forces from cell boundary deformation and mechanical characterization of the embryo can be realized. This can be used in an automatic microinjection if microassembly workstation is modified for such a task.

Bibliography

[1] K.F. Bohringer, R.S. Fearing, and K.Y. Goldberg, Handbook of Industrial Robotics, Microassembly Chapter. New York, John Wiley and Sons, 1999, 1045-1066.

[2] B. Nelson, Y. Zhou, and B. Vikramaditya, Sensor-based microassembly of hybrid MEMS devices, *IEEE Control Systems Magazine*, 18(6), 1998, 35-45.

[3] A.H. Slocum, Precision Machine Design, Prentice Hall, 1992.

[4] R.S. Fearing, A Planar Milli-Robot System on an Air Bearing, *Robotics Research the 7th International Symposium*, edited by G. Giralt and G. Hirzinger, London, Springer-Verlag, 1996, 570-581.

[5] I. Shimoyama, Scaling in microrobotics, *IEEE/RSJ Int. Workshop on Intelligent Robots and Systems (IROS)*, Pittsburgh, PA, 1995, 208-211.

[6] R.S. Fearing, Survey of Sticking Effects for Micro Parts Handling, *IEEE/RSJ Int. Workshop on Intelligent Robots and Systems (IROS)*, Pittsburgh, PA, 1995, 212-217.

[7] S. Hutchinson, G.D. Hager, and P.I. Corke, A Tutorial on Visual Servo Control, *IEEE Transactions on Robotics and Automation*, 12(5), 1996, 651-670.

[8] D. Kragic, H.I. Christensen, Survey on visual servoing for manipulation, Technical Report, 2002.

[9] F. Chaumette, S. Hutchinson, Visual Servo Control - Part II: Advanced Approaches, IEEE Robotics and Automation Magazine, 14(1), 2007, 109-118.

[10] Y. Mezouar, P. K. Allen, Visual Servoed Micropositioning for Protein Manipulation Tasks, *IEEE Conf. on Intelligent Robots and Systems*, Switzerland, 2002, 1766-1771.

[11] S.J. Ralis, B. Vikramaditya, and B.J. Nelson, Micropositioning of A Weakly Calibrated Microassembly System Using Coarse-to-Fine Visual Servoing Strategies, *IEEE Trans. On Electronics Packing Manufacturing*, 23, 2000, 123-131.

[12] R.Y. Tsai, A Versatile Camera Calibration Technique for High-Accuracy 3D Machine Vision Metrology Using Off-the-Shelf TV Cameras and Lenses, *IEEE Journal of Robotics and Automation*, 3(4), 1987, 323-344.

[13] Z.Y. Zhang, Flexible Camera Calibration by Viewing a Plane from Unknown Orientations, *IEEE International Conference on Computer Vision*, 1999, 666-673.

[14] B. Caprile, V. Torre, Using Vanishing Points for Camera Calibration, *International Journal on Computer Vision*, 4(2), 1990, 127-140.

[15] H. Zhuang and W.C. Wu, Camera Calibration with a Near-Parallel Calibration Board Configuration, *IEEE Transactions on Robotics and Automation*, 12(6), 1996, 918-921.

[16] Y. Zhou, B.J. Nelson, Calibration of a parametric model of an optical microscope, *Optical Engineering*, 38, 1999, 1989-1995.

[17] M. Ammi, V. Fremont, A. Ferreira, Flexible Microscope Calibration using Virtual Pattern for 3-D Telemicromanipulation, *IEEE Transactions on Robotics and Automation*, 2005, 3888-3893.

[18] J. Flusser, B. Zitova, Invariants to Convolution with Circularly Symmetric PSF, *IEEE International Conference on Pattern Recognition*, 2004, 11-14.

[19] S. Benhimane and E. Malis, Real-time image-based tracking of planes using Efficient Second Order Minimization, *IEEE/RSJ International Conference on Intelligent Robots and Systems*, 1, 2004, 943-948.

[20] S.K. Nayar, Y. Nakagawa, Shape from Focus, *IEEE Transactions on Pattern Analysis and Machine Intelligence*, 16(8), 1994, 824-831.

[21] J. Yun, T.-S. Choi, Accurate 3-D shape recovery using curved window focus measure, *IEEE International Conference on Image Processing*, 1999, 910914.

[22] F.S. Helmli, S. Scherer, Adaptive Shape from Focus with an Error Estimation in Light Microscopy, *Second International Symposium on Image and Signal Processing and Analysis*, 2001, 188-193.

[23] A.S. Malik, T.-S. Choi, Consideration of illumination effects and optimization of window size for accurate calculation of depth map for 3D shape recovery, *Pattern Recognition*, 40, 2007, 154-170.

[24] A.S. Malik, S.-O. Shim, T.-S. Choi, Depth Map Estimation using a Robust Focus Measure, *IEEE International Conference on Image Processing*, 2007, 564-567.

[25] J. Niederoest, M. Niederoest, J. Scucka, Shape from focus: fully automated 3d reconstruction and visualization of microscopic objects, *Proceedings of 6th International Conference on Optical 3-D Measurement Techniques*, 2003, 4-11.

[26] A. Pentland, A new sense for depth of field, *IEEE Trans. Pattern Analysis and Machine Intell.*, 9(4), 1987, 523-531.

[27] K.S. Pradeep, A.N. Rajagopalan, Improving Shape from Focus Using Defocus Cue, *IEEE Transactions on Image Processing*, 16(7), 2007, 1920-1925.

[28] P.J. Besl, R.C. Jain, Segmentation Through Variable-Order Surface Fitting, *IEEE Transactions on Pattern Analysis and Machine Intelligence*, 10(2), 1988, 167-192.

[29] E. Trucco, A. Verri, Introductory Techniques for 3-D Computer Vision. New Jersey, Prentice Hall, 1998.

[30] E. Trucco, R.B. Fisher, Experiments in Curvature-Based Segmentation of Range Data, *IEEE Transactions on Pattern Analysis and Machine Intelligence*, 17(2), 1995, 177-182.

[31] A.B. Moreno, A. Sanchez, J.F. Velez, and F.J. Diaz, Face recognition using 3D surface-extracted descriptors, *Proceedings of Irish Machine Vision and Image Processing Conference*, 2003.

[32] H. Hertz, On the contact of elastic solids, *J. Reine Agnew. Math.*, 92, 1881.

[33] I.N. Sneddon, The relationship between load and penetration in the axisymmetric boussinesq problem for a punch of arbitrary profile, *Int. J. Eng. Sci.*, 3, 1965, 47-57.

[34] J.M. Mitchison, M.M. Swann, The mechanical properties of the cell surface: I. the cell elastimeter, *J. Exp. Biol.*, 31, 1954, 443-460.

[35] Y. Sun, K.-T. Wan, K.P. Roberts, J.C. Bischof, and B.J. Nelson, Mechanical Property Characterization of Mouse Zona Pellucida, *IEEE Transactions on Nanobioscience*, 2(4), 2003, 279-286.

[36] D.-H. Kim, Y. Sun, S. Yun, B. Kim, C.N. Hwang, S.H. Lee, and B.J. Nelson, Mechanical Property Characterization of the Zebrafish Embryo Chorion, *Proceedings of the 26th Annual International Conference of the IEEE EMBS*, 2004, 5061-5064.

[37] K.T. Wan, V. Chan, and D.A. Dillard, Constitutive equation for elastic indentation of a thin-walled bio-mimetic microcapsule by an atomic force microscope tip, *Colloids Surf. B: Biointerfaces*, 27, 2002, 241-248.

[38] K.T. Wan and K.K. Liu, Contact Mechanics of a thin-walled capsule adhered onto a rigid planar substrate, *Med. Biol. Eng. Comput.*, 39, 2001, 605-608.

[39] C. Dietrich, M. Angelova, and B. Pouligny, Adhesion of latex spheres to giant phospholipid vesicles: Statics and dynamics, *J. Phys. II France*, 7, 1997, 1651-1682.